VCSEL AND INTEGRATION TECHNIQUES FOR WAVELENGTH-MULTIPLEXED OPTICAL INTERCONNECTS

Mehdi Jahed

CHALMERS

VCSEL and Integration Techniques For Wavelength-Multiplexed Optical Interconnects
Mehdi Jahed
©Mehdi Jahed, 2021

Chalmers University of Technology
Department of Microtechnology and Nanoscience - MC2
Photonics Laboratory
SE–412 96 Göteborg
Sweden
Phone: +46–(0)31–772 10 00

Front cover illustration: Microscopic image of the fabricated monolithic multi-wavelength VCSEL array with uniform static performance (Left) and microscopic image of the VCEL-to-photodetector optical link (Right).

VCSEL and Integration Techniques for Wavelength-Multiplexed Optical Interconnects
Mehdi Jahed
Photonics Laboratory
Department of Microtechnology and Nanoscience
Chalmers University of Technology

Abstract

GaAs-based vertical-cavity surface-emitting lasers (VCSELs) are dominating short-reach optical interconnects (OIs) due to their high modulation speed, low power consumption, circular output beam and low fabrication cost. Such OIs provide the high bandwidth connectivity needed for interconnecting servers and switches in data centers. With the rapidly increasing use of Internet-based applications and services, higher bandwidth connectivity and higher aggregate capacity VCSEL-based OIs are needed. Until now, this has been achieved mostly through an increase of the lane rate by higher speed VCSELs and higher order modulation formats. Furthermore, spatial-division-multiplexing has proven effective for increasing the aggregate capacity. Much higher capacity can be achieved by multiple wavelengths per fiber, known as wavelength-division-multiplexing (WDM). Moreover, smaller footprint and higher bandwidth density WDM transceivers can be built using monolithic multi-wavelength VCSEL arrays with densely spaced VCSELs. This requires a VCSEL technology where the wavelength of individual VCSELs can be precisely set in a post-epitaxial growth fabrication process and a photonic integrated circuit (PIC) for multiplexing and fiber coupling. Flip-chip integration over grating couplers (GCs) is considered for interfacing VCSELs with waveguides on the PIC.

In this thesis, an intra-cavity phase tuning technique is demonstrated for setting the resonance wavelength of VCSELs in a monolithic array with an accuracy in spacing of <1 nm. Uniform performance over the array is achieved by spectral matching and balancing of mirror reflectances, optical confinement factor and optical gain. Single transverse and polarization mode VCSELs, as required for flip-chip integration over GCs, with a record output power of 6 mW are also demonstrated.

Finally, an investigation of angled flip-chip integration of a VCSEL over a GC on a silicon photonic integrated circuit (Si-PIC) is presented. Dependencies of coupling efficiency and optical feedback on flip-chip angle and size of the VCSEL die are studied using numerical FDTD simulations. Moreover, flip-chip integration of a VCSEL over a GC on a Si-PIC is experimentally demonstrated. The insertion loss from the VCSEL at the input GC to a singlemode fiber, multimode fiber or flip-chip integrated photodetector over the output GC was measured and quantified. The latter forms an on-PIC optical link.

Keywords: optical interconnects, wavelength-division-multiplexing, vertical-cavity surface-emitting laser, wavelength setting, mode control, flip-chip integration, silicon photonics

List of appended papers

This thesis is based on the following appended papers:

[A] **M. Jahed**, J. S. Gustavsson, and A. Larsson, " Precise setting of micro-cavity resonance wavelength by dry etching", *Journal of Vacuum Science and Technology B, Nanotechnology and Microelectronics: Materials, Processing, Measurement, and Phenomena*, vol. 37(3), 031217, May 2019. DOI: 10.1116/1.5092192

[B] **M. Jahed**, J. S. Gustavsson, and A. Larsson, "VCSEL wavelength setting by intra-cavity phase tuning–numerical analysis and experimental verification", *IEEE Journal of Quantum Electronics*, vol. 57, no. 6, 2400307, Dec. 2021. DOI: 10.1109/JQE.2021.3119104

[C] **M. Jahed**, J. S. Gustavsson, and A. Larsson, "Monolithic multi-wavelength VCSEL arrays with uniform performance by intra-cavity phase tuning", *27th IEEE International Semiconductor Laser Conference (ISLC)*, Potsdam, Germany, Oct. 10-14, 2021.

[D] E. Haglund, **M. Jahed**, J. S. Gustavsson, A. Larsson,J. Goyvaerts, R. Baets, G. Roelkens, M. Rensing, and P. O'Brien "High-power single transverse and polarization mode VCSEL for silicon photonics integration", *Optics Express*, vol. 27, no. 13, pp. 18892-18899, June 2019. DOI:101364/OE.27.018892.

[E] **M. Jahed**, A. Caut, J. Goyvaerts, M. Rensing, M. Karlsson, A. Larsson, G. Roelkens, R. Baets, and P. O´Brien, "Angled flip-chip integration of VCSELs on silicon photonic integrated circuits", *Manuscript*.

Related conference contribution by the author not included in this thesis:

[F] **M. Jahed**, J. S. Gustavsson, and A. Larsson, "Precise setting of VC-SEL resonance wavelength by dry etching", *21st International Vacuum Congress (IVC-21)*, Jul. 1-5, 2019.

Contents

Acknowledgement

Many people have supported me during this work and deserve for my gratitude. First of all, I would like to thank my supervisor Prof. Anders Larsson for giving me the opportunity to work in this exciting field, his excellent support and fruitful discussions. I am grateful to my assistant supervisor Assoc. Prof. Johan Gustavsson for his simulations, fruitful discussions and support. I am also grateful to my examiner, Prof. Åsa Haglund. I would like to thank Dr. Emanuel P. Haglund for a perfect introduction to VCSEL fabrication, measurement techniques and sharing his knowledge with me. Dr. Erik Haglund deserves my gratitude for always sharing his vast knowledge in VCSEL fabrication and measurement, Dr. Ewa Simpanen and Alexander Grabowski for always being there for discussion, characterization, and fabrication. I also would like to thank internal collaborators, Prof. Magnus Karlsson, Prof. Victor Torres Company, Marcello Girardi, and Alexander Caut for excellent discussions and simulations on Integrated Silicon Photonics.

Furthermore, I would like to acknowledge all excellent external collaborators at Photonics Research Group in Ghent University-Imec and Tyndall National Institute. Special thanks to Dr. Marc Rensing for perfect flip-chipping of VCSELs and photodetectors and Dr. Jeroen Goyvaerts for photonics integrated circuits design and simulation.

I am honored to be a member of Photonics Lab, had and have so many wonderful friends and colleagues who make such a nice environment to work and many memorable moments. Thank you, Dr. Michael Alexander Bergmann, Dr. Filip Hjort, and Marcello for nice discussions on fabrication processes at the cleanroom. Thank you, Jeanette and Gunnel, for being such an excellent and nice secretary. I also would like to thank Nanofabrication Laboratory staff for their excellent support, sharing knowledge and keeping the tools at the best performance.

Last, but not least I would like to express my gratitude from deepest part of my heart to my family, my parents, Parvin and Emran. Sahar, my beloved wife, you mean everything to me. I could not have made it without you always being there for me.

Mehdi Jahed

Göteborg
November 2021

x

List of abbreviations

AFM	atomic force microscopy
AR	anti-reflection
BCB	benzocyclobutene
BER	bit-error-rate
BTJ	buried tunnel junction
CCD	charge coupled device
CMOS	complementary metal-oxide-semiconductor
CW	continuous-wave
CWDM	coarse wavelength division multiplexing
DBR	distributed Bragg reflector
DEMUX	demultiplexer
DMT	discrete multitone
DWDM	dense wavelength division multiplexing
EEL	edge emitting laser
FEC	forward error correction
GC	grating coupler
LED	light emitting diode
MCF	multicore fiber
MM	multimode
MMF	multimode fiber
MOCVD	metal-organic chemical-vapor deposition
MQW	multiple quantum well
MUX	multiplexer
NA	numerical aperture
NRZ	non-return-to-zero
OI	optical interconnect
OOK	on-off keying
OSA	optical spectrum analyzer
PAM-4	4-level pulse amplitude modulation
PD	photodetector
PIC	photonic integrated circuit
QW	quantum well
SDM	spatial division multiplexing

SiP	silicon photonics
SM	singlemode
SMF	single-mode fiber
SOI	silicon-on-insulator
SPM	scanning probe microscopy
TIA	transimpedance amplifier
ToR	top-of-rack
VCSEL	vertical-cavity surface-emitting laser
VNA	vector network analyzer
VOA	variable optical attenuator
WDM	wavelength division multiplexing

Chapter 1

Introduction

In March 2021, 65.6% of the world population used the Internet, while it was 56.8% in 2019. The world population of Internet users in 2021 has grown by 13.3 times compared to year 2000 and reached 5,168,780,607 in March 2021. The maximum growth $(130, 58\%)$ is in Africa and 53.4% of the Internet users live in Asia. 93.9% and 88.2% of the Northern America and Europe, respectively, use Internet [1]. Every day we use the Internet to connect with friends and family, stream music and movies, share ideas and knowledge, search for information, shop online, etc. It is difficult to imagine the world without the Internet.

Two key components of the Internet infrastructure are optical fiber cables and data centers. Vast amounts of data are transmitted through these cables across the world while data is being processed, stored, and accessed in data centers. With increasing use of Internet-based applications and cloud computing, the number of the data centers and their size increase rapidly. Moreover, our computers, smartphones, and tablets are mainly used as terminals where we access information, while data storage and processing are located in the data centers. The number of hyperscale data centers was 259 in 2015 and was predicted to be 485 in 2020 [2] but reached to 597 [3]. The largest data center in the world had a size of 100,000 m^2 (equivalent to 12 FIFA standard football fields) in 2015 [4] and 1,000,000 m^2 in 2019 [5] (nearly 120 football fields). This up-scaling means that present and future data centers, as well as supercomputers, need an internal communication network with huge capacity. Both longer reach (up to 2 km) and shorter-reach (meter's) optical interconnects (OIs) are needed when data centers increase in size and when OIs are increasingly used in the server racks. GaAs-based vertical-cavity surface-emitting lasers (VCSELs), offering low cost, low power consumption, small footprint, high modulation speed at low current, and excellent reliability, are well-suited for short-reach OIs in particular [6, 7].

1.1 Data center architecture

Data centers, either room-scale or hyperscale, are made of cabinets of servers and since the number of hyperscale data centers is increasing and they are the main hubs for the global data traffic, in this section, the architecture of a hyperscale data center is introduced. In the hyperscale data center, there are numerous racks of stacked servers and storage units clustered in pods. Each rack contains multiple servers or storage units. A top-of-rack (ToR) switch interconnects all units within the rack. The ToR switch, e.g., a gigabit Ethernet switch, can be put anywhere in the rack, not just limited to the top. However, engineers prefer to have the ToR at the top for easier accessibility and cleaner cable management, Figure 1.1

Moreover, the ToR switches are connected using additional layers of network switches. The way switches are connected to each other is called topology. In a hyperscale data center, careful consideration of topology is necessary due to network throughput, latency, congestion, and packet loss [9, 10]. Furthermore, the up-scale topology needs to support a large inter-node communication bandwidth. The fat-tree topology was proposed for fulfilling these requirements [11]. A simplified view of a fat-tree topology is shown in Figure 1.2. The motivation behind the fat-tree topology is achieving maximum bisection bandwidth in the network, which requires spreading outgoing traffic from any given pod as evenly as possible among the core switches. The fat-tree topology provides large bisectional bandwidth, economical scalability, low power consumption, and backward compatibility in large data centers [10–13].

In addition, todays, interconnects employ optical fibers instead of copper cables. They provide higher data rates with large bandwidth, minimum attenuation, and low power consumption [14], and there is no crosstalk or any
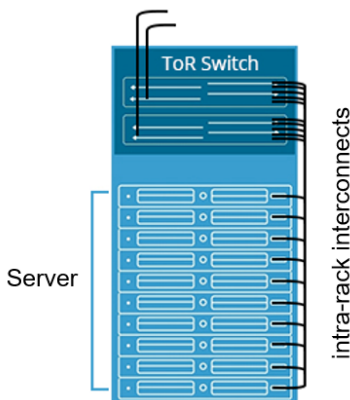
Figure 1.1: A schematic view of a rack of servers. Each server connects to the ToR switch via intra-rack interconnects [8].
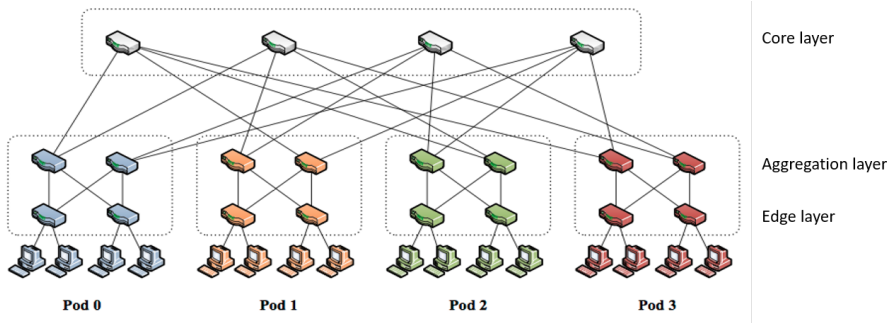
Figure 1.2: Simplified view of a fat-tree topology. Core layer switches are on top and connect to each server in pods via aggregation layer and edge layer switches [11].

electromagnetic interference [15,16]. The most common OI consists of a GaAs-based VCSEL operating at 850 nm with a multimode fiber (MMF) [12].

1.2 Toward higher capacity data center connectivity

The 850 nm GaAs-based VCSEL technology is used in 95% of all optical networking applications with reach <1000 m [17]. In a data center, 850 nm VCSELs are used as the light source in short-reach OIs (intra-rack and lower-level network). However, as the throughput of servers and switches increases, the increasing number of transceivers in a limit space presents a formidable challenge. Hence, there is a great need for OI transceivers with higher capacity and higher bandwidth density [18].

Large efforts have been invested in the development of higher aggregate capacity OIs. On-off-keying, non-return-to-zero (OOK-NRZ) data transmission up to 57 Gbit/s at 25°C and 50 Gbit/s at 85°C, without equalization or forward-error-correction (FEC), has been achieved using 850 nm VCSELs [19]. With transmitter and receiver equalization, error-free data rates >70 Gbit/s have been demonstrated [20]. More recently, 1060 nm single and multimode VCSELs (GaAs-based) were investigated for extending the reach of VCSEL-based OIs [21]. Extended reach is enabled by the lower fiber chromatic dispersion and attenuation at longer wavelengths [22]. To further increase capacity, higher order modulation formats are used. The PAM-4 format is of primary interest because of low power consumption and low complexity. PAM-4 with transmitter equalization and pulse shaping has enabled error-free (no FEC) 100 Gbit/s transmission over 100 m MMF at both 850 and 1060 nm [23, 24].Further improvements of aggregate capacity, and bandwidth density, may come from the use of multiple cores per fiber (spatial division multiplexing, SDM) or multiple

wavelengths per fiber (wavelength division multiplexing, WDM). A multicore fiber (MCF) interconnect with a single fiber capacity of 240 Gbit/s has been demonstrated using a 6-core fiber and a 6-element VCSEL array [25]. Coarse WDM (CWDM) with 4 channels and 30 nm channel spacing (850, 880, 910, and 940 nm), known as SWDM4, is being implemented [26] and has demonstrated up to 400 Gbit/s (4 × 100 Gbit/s) single fiber capacity [27]. With WDM being the most promising and scalable approach for higher aggregate capacity and higher bandwidth density, increasing the number of wavelengths per fiber from 4 to 8 and beyond is considered to increase the capacity on a single fiber to ~ 1 Tbit/s and the aggregate capacity on multiple fibers to ~ 10 Tbit/s [28].

1.3   VCSEL-based optical interconnects

A schematic of a VCSEL-based single-channel OI is shown in Figure 1.3. It is composed of a transmitter, an optical fiber, and a receiver. The VCSEL-based transmitter consists of a VCSEL, which is directly modulated by a driver to convert the input electrical signal to an optical signal transmitted along the optical fiber. At the receiver, the received signal is converted back to the electrical domain by a photodetector (PD), a transimpedance amplifier (TIA) and subsequently amplified to a sufficient level.

Short-reach (<300 m) OI transmitters predominantly employ 850 nm GaAs-based VCSELs [6]. For longer reach, VCSELs emitting at longer wavelengths can be employed. The VCSEL emission wavelength depends on the semiconductor compounds used in the VCSEL structure. In the GaAs-based VCSEL, with AlGaAs compounds in the mirrors and InGaAs compounds in the active region, the wavelength can be extended to ~ 1100 nm [29]. For longer wavelength VCSELs at 1310 and 1550 nm, InP-based compounds are used. However, while optical fiber performance is optimum at 1310 nm (minimum chromatic dispersion) and 1550 nm (minimum attenuation), InP-based VCSELs suffer from higher threshold currents due to a higher non-radiative recombination rate [30] and more complex mirror designs due to the small refractive index contrast offered by the InP-based compounds.

The optical fiber link provides broad bandwidth transmission, low cost, light weight, high security, and immunity to electromagnetic interference compared to the copper cables. Its attenuation is low but wavelength dependent, 2 dB/km
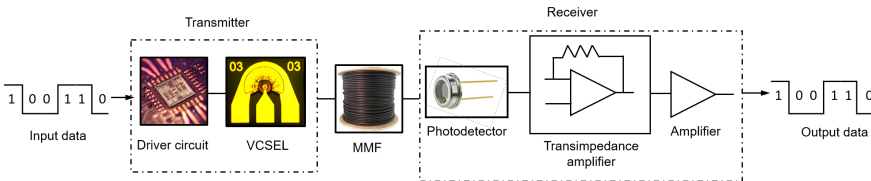
Figure 1.3: Single-channel VCSEL-based OI.

at 850 nm and 0.2 dB/km at 1550 nm [22]. The MMF used in OIs is more expensive than the singlemode fiber (SMF) due to its complex refractive index profile [31] but offers relaxed alignment tolerance to the light source because of its large core size. Singlemode technology (SMF and singlemode VCSEL) can be used to extend reach, but it needs more critical alignment and therefore increases assembly and packaging cost.

1.4   Outline of thesis

This thesis is outlined as follows. In Chapter 2, dense WDM (DWDM) and course WDM (CWDM) for OIs are introduced along with the demand for any kind of multiplexing technique to achieve higher bandwidth density and higher aggregate capacity. Moreover, it defines the requirements on a VCSEL for integration in a CWDM transceiver. Chapter 3 introduces the VCSEL design and its various building blocks, along with its basic static and dynamic characteristics and associated performance measures. VCSEL wavelength setting by intra-cavity phase tuning and the uniformity limitations of monolithic multi-wavelength VCSEL arrays, in terms of static and dynamic performance together with fabrication and testing results are discussed and reviewed in Chapter 4. In addition, a mode filtering technique for controlling the transverse and polarization mode properties is introduced in this chapter. In Chapter 5, different techniques for light source integration on silicon photonic integrated circuits (Si-PIC) are reviewed. Also, flip-chip integration of VCSELs and the condition under which a VCSEL can be integrated are discussed. Experimental results from a VCSEL-to-PD optical link on a PIC is presented. In Chapter 6, most important and critical steps for fabricating a high-performance monolithic multi-wavelength intra-cavity contacted VCSEL array is presented. Finally, a future outlook and summary of appended papers are given in Chapters 7 and 8, respectively.

Chapter 2

Wavelength multiplexed optical interconnects

The performance of a data center has become largely limited by the capacity and efficiency of the networks used to interconnect servers, storage units, and switches. Future data centers with very large scale and bandwidth will need networks with very high aggregate capacity (a thousand times higher than today's maximum capacity). In addition to higher speed VCSELs (with baud rates of 50 and 100 Gbaud/s) together with higher order modulation formats (PAM-4, PAM-8, DMT, duobinary ...) for higher lane rates, multiplexing is needed for very high aggregate capacity. SDM employs parallel fibers or a MCF to transmit one channel per fiber core and therefore multiplies the net capacity. Until now, higher OI capacity has been achieved predominantly through an increase of the lane rate and using parallel fibers [25]. Future large-scale data centers will require multi-Tbit/s interconnect capacity and major improvements of bandwidth density. However, current OI technologies are expected to saturate at the ~ 1 Tbit/s level. WDM, with multiple channels at different wavelengths on a single fiber core, is considered the solution for reaching multi-Tbit/s capacity.

2.1 Dense and coarse WDM

In a WDM system, see Figure 2.1, several signals at different wavelengths emitted by different lasers, are combined in a multiplexer (MUX) and transmitted together through a single fiber with a single core. At the receiver, they are split by a demultiplexer (DEMUX) and detected by an array of PDs. Thereby, interconnect capacity can be increased without increasing the number of optical fibers [32]. This also improves the bandwidth density.

WDM systems are classified according to the spectral density of multiplexed channels. VCSEL-based SWDM4 OIs, with direct modulation and direct de-
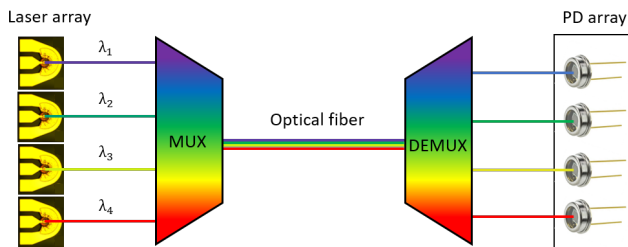
**Figure 2.1:** Four-channel WDM system.

tection, use a channel spacing of 30 nm and four discrete VCSELs emitting at different wavelengths. This is referred to as coarse WDM. The large channel spacing simplifies system implementation and accommodates the drift in wavelength with temperature ($\sim$ 4 nm from 25°C to 70°C for a GaAs-based VCSEL at $\sim$ 1000 nm) . In long haul optical communication systems, dense WDM (DWDM) is used. Here, the channel spacing is much smaller and the number of channels is much larger, e.g., 80 channels with 50 GHz spacing. This requires the use of coherent techniques for encoding and decoding of data on the optical carriers.

2.2 VCSEL-based WDM interconnects

In data center servers and switches, as well as the data processing and storage equipment used in supercomputers, there is a large number of OI transceivers in a limited space. Therefore, bandwidth density, quantified by the Gbit/s/mm figure of merit, is an important measure [33]. Any form of multiplexing (SDM or WDM) of the interconnect channels, which could improve bandwidth density, is therefore of interest. The maximum achievable capacity of VCSEL-based OIs using SDM is considered to be at the $\sim$ 1 Tbit/s level. However, future data centers will need at least an order of magnitude higher capacity and this can potentially be provided by WDM. The use of discrete VCSELs emitting at different wavelengths (e.g., SWDM4) can be used to build WDM transmitters but the use of discrete components increases the footprint and limits the bandwidth density. With monolithic multi-wavelength arrays of VCSELs, both high aggregate capacity and high bandwidth density can be achieved [32].

2.2.1 Monolithic multi-wavelength VCSEL arrays – state-of-the-art

The resonance wavelength of a VCSEL is set by the phase of the reflections from the distributed Bragg reflectors (DBRs) and the propagation phase delay in the cavity separating the DBRs. The latter is controlled by the optical length of the cavity. Therefore, both reflection phases and cavity length are
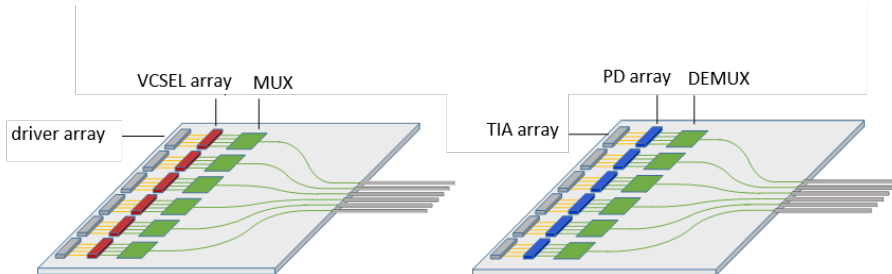
Figure 2.2: Left: SiP transmitter with flip-chip mounted multi-wavelength VCSEL arrays, multi-channel drivers and integrated MUXs. Right: SiP receiver with flip-chip mounted PD arrays, multi-channel TIAs and integrated DEMUXs.

parameters that can be used to set the resonance wavelength of VCSELs in a multi-wavelength VCSEL array.

Since the early 1990's, different techniques for fabricating monolithic multi-wavelength VCSEL arrays have been explored. Non-uniform [34] and non-planar [35] epitaxial growth were used to induce a variation in cavity length, and therefore wavelength, over the wafer. However, VCSEL designs and fabrication techniques that allow for post-growth wavelength setting are preferred for precisely controlling the emission wavelength of VCSELs at specific locations on the wafer. Among these techniques, non-planar bonding to control the cavity length of wafer bonded VCSEL [36], selective oxidation for modifying the cavity length [37, 38], replacement of the top-DBR by a high-contrast grating to control the reflection phase by the grating parameters [39], the use of an intra-DBR phase tuning layer for controlling the DBR reflection phase [40–44], and the use of an intra-cavity phase tuning layer for controlling the cavity length [45, 46] have been explored. While VCSELs are predominantly considered for CWDM with intensity modulation and direct detection, there are exceptions. For instance, in [47] a monolithic InP-based VCSEL array with wavelengths set by intra-cavity phase tuning to a channel spacing of 100 GHz was used to enable a 100 Gbit/s per channel using polarization-division-multiplexed PAM-4 and coherent detection for an aggregate capacity of 400 Gbit/s.

2.2.2 Integrated CWDM transceivers

The construction of compact CWDM transmitters with small footprint and high bandwidth density requires an integration platform on which multi-wavelength VCSEL arrays and multi-channel drivers can be mounted, and the different wavelength channels can be multiplexed and coupled to a single fiber. A similar integration platform is needed for the receiver, with a DEMUX and arrays of PDs and TIAs. We envision using a complementary metal-oxide-semiconductor (CMOS) compatible silicon photonics (SiP) integration platform
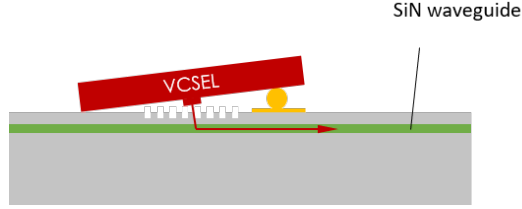
Figure 2.3: Flip-chip integration of a VCSEL at an angle over a GC in the SiN waveguide.

for this purpose, Figure 2.2. Such platforms, with silicon-on-insulator (SOI) waveguides for wavelengths >1100 nm and silicon nitride (SiN) waveguides for wavelengths <1100 nm, are available with low waveguide loss and low loss MUXs and DEMUXs [48].

Flip-chip integration of VCSELs at an angle over grating couplers (GCs) Figure 2.3, enable independent optimization of VCSEL performance. The tilt eliminates optical feedback to the VCSEL and facilitates unidirectional coupling to the waveguide without the need for e.g., a slanted grating coupler.

2.2.3 VCSEL requirements

While flip-chip integration of a VCSEL over a GC on the Si-PIC offers certain advantages [49, 50] it is also demanding in terms of the modal properties of the VCSEL, in addition to the wavelength having to be precisely controlled. Since the GC is polarization sensitive and with the waveguide being singlemode, the VCSEL has to be single (fundamental) transverse mode with a stable and linear polarization state. In addition, to overcome optical losses in the different parts of the SiP circuit (GCs, MUXs, DEMUXs, and fiber couplers), high output power from the VCSEL is required.

To fabricate a single transverse mode oxide-confined VCSEL, different approaches are available. Since the number of transverse modes is controlled by the size of the oxide aperture, a small aperture ($< \sim 3$ µm) results in single transverse mode operation. However, small aperture VCSELs have high electrical and thermal resistance and therefore limited output power. Higher power can be achieved with a larger aperture (lower resistance) and a mode filter etched into the surface of the VCSEL. With a proper size of the mode filter with respect to the aperture, higher order transverse modes can be suppressed and singlemode emission with >30 dB suppression of higher order modes can be achieved [51]. With a grating in the mode filter, the polarization can also be pinned for >20 dB suppression of the orthogonal polarization mode [52]. If the grating pitch is sub-wavelength, beam degradation due to diffraction is avoided [53].

Chapter 3

Vertical-cavity surface-emitting lasers

LASER is an acronym for "Light Amplification by Stimulated Emission of Radiation" and describes amplification of a light wave as it propagates inside a medium with population inversion. Generally, a laser is made of a gain medium confined inside an optical resonator (cavity) which itself is composed of two semitransparent mirrors. To establish population inversion for optical gain, and therefore light amplification, energy has to be supplied to the gain medium. In a semiconductor laser, the light wave is amplified through the stimulated emission process in an inverted semiconductor material. The emission from a laser is coherent and therefore spectrally pure. Lasers have found many applications e.g., in medicine, communication, manufacturing, and spectroscopy.

The first laser, an optically pumped ruby crystal, was demonstrated by Theodor Maiman in 1960 [54]. Since that day, many kinds of laser with different size and power for different applications have been demonstrated. Today, nanoscale size lasers [55] are well established. The largest laser, with size of three football fields and located at the National Ignition Facility in the United States, delivers nearly 2 million joules of ultra-violet laser energy in billionth of a second pulses for fusion research [56].

The VCSEL concept was proposed by Professor K. Iga in 1977 [57] and demonstrated experimentally in 1979 by Soda and Iga, et. al [58]. The first room temperature, continuous-wave VCSEL was demonstrated in 1988 [59]. One year later, in 1989, the first low-threshold current (near 1 mA) VCSEL was independently demonstrated by Jewell and Lee [60,61]. Moreover, the first sub-mA threshold current VCSEL was demonstrated by the group of Professor Coldren in 1990 [62,63].

3.1 Concept and basic performance

The VCSEL is a semiconductor laser in which the light inside the resonator oscillates in the direction perpendicular to the active region plane. Therefore, light is emitted from the surface of the wafer, Figure 3.1.a. The resonator consists of an active region sandwiched between two mirrors. The active region contains a direct bandgap semiconductor material embedded in higher bandgap material. The mirrors are p- and n-type highly reflective (99%) DBRs. Optical gain is established when the pn-junction is forward biased.

In contrast to the VCSEL, the edge-emitting laser (EEL) has a horizontal resonator and emits light from cleaved semiconductor-air facets, Figure 3.1.b. In the edge-emitting Fabry-Perot laser, the cleaved facets act as mirrors. Coatings can be applied to the facets to control the amount of light emitted from each facet. Therefore, an EEL wafer has to be cleaved before lasers can be tested. On the contrary, all VCSELs on a VCSEL wafer can be tested and screened on wafer before scribe and break into separate VCSEL dies. This greatly reduces the cost for laser manufacturing. Because of the vertical geometry, VCSELs can also be integrated in large 2D arrays.

3.1.1 Active region – optical gain and spontaneous emission

In a semiconductor laser, the gain medium is, in its most simple form, a thin un-doped direct bandgap layer (active region) sandwiched between higher bandgap layers embedded in a pn-junction for current injection and population of states in the conduction and valence bands by electrons and holes, respectively. Band-to-band transitions in the active region can be divided into radiative and non-radiative. In a radiative transition, an electron can make either an upward
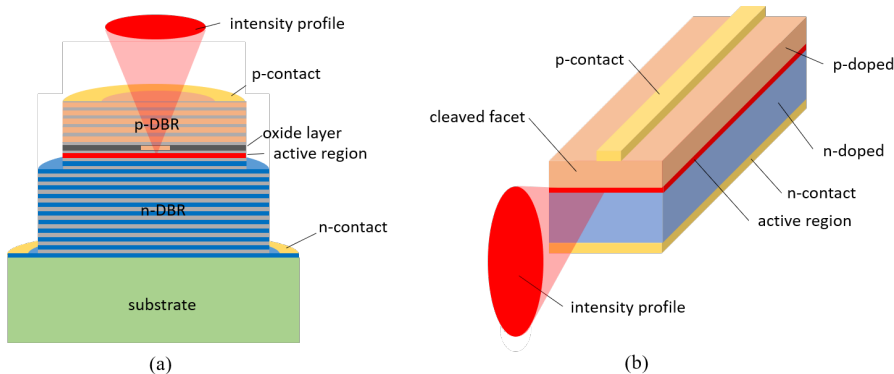
Figure 3.1: Geometry and optical output of (a) an oxide-confined VCSEL and (b) an edge emitting stripe laser.

transition from a valence band state to a conduction band state by absorbing a photon or a downward transition from a conduction band state to a valence band state by emitting a photon. In contrast, in a non-radiative transition phonons are emitted rather than a photon in the downward transition, which generates heat in the crystal. Radiative transitions are fundamental for opto-electronic light emitters and detectors.

Radiative transition can be divided into stimulated and spontaneous:

- Stimulated absorption (commonly referred to as absorption only) in which an electron absorbs a photon and makes a transition from a valence band state to a conduction band state, leave a hole in the valence band state.

- Stimulated emission in which an electron in a conduction band state is stimulated by a photon to make a transition to an empty valence band state, thereby generating a second photon with the same frequency, phase, and propagation direction (coherent radiation). This requires a non-equilibrium condition, established by carrier injection in the forward biased pn-junction.

- Spontaneous emission in which a photon is generated when an electron in a conduction band state makes a spontaneous transition to an empty state in the valence band. The photons generated have random phase and propagation direction and are spread spectrally (incoherent radiation).

The radiative spontaneous emission process involves an electron in the conduction band and a hole in the valence band. The transition rate is therefore proportional to the product of the non-equilibrium electron and hole concentrations. Under the assumption of charge neutrality, these are equal. Non-radiative transitions are caused by crystal imperfections due to defects and impurities and surface and interface states. The associated transition rate is directly proportional to the non-equilibrium electron concentration. Non-radiative transitions can also occur when non-equilibrium electrons and holes recombine to excite and electron to a higher energy state in the conduction band. This is referred to as Auger recombination. Since this involves two electrons and one hole, the associated transition rate has a cubic dependence on the non-equilibrium carrier concentration. As a result, the total spontaneous recombination rate, $R_{sp}(\Delta n)$, becomes [64]:

$$R_{sp}(\Delta n) = A \cdot \Delta n + B \cdot \Delta n^2 + C \cdot \Delta n^3, \qquad (3.1)$$

where Δn is the concentration of excess electrons and holes, assumed equal. The first and third terms represent non-radiative defect related and Auger recombination, respectively. The second term represents the radiative spontaneous emission process, which generates photons. Spontaneous emission is the process that initiates lasing in a semiconductor laser.

We next consider the stimulated transition rates. Under equilibrium, with filled valence band states and empty conduction band states, only upward transitions (absorption) can occur. Under non-equilibrium, where states in the

conduction band are populated and states in the valence band are emptied by carrier injection, both upward and downward transitions occur. At sufficient injection, population inversion occurs and the downward transition rate exceeds the upward. This leads to net stimulated emission and optical gain, another essential ingredient in semiconductor lasers. With increasing current through the forward biased pn-junction, and therefore increasing carrier density in the active region, the spontaneous and stimulated emission rates increase. At a certain current and carrier density, referred to as the threshold current and the threshold carrier density, the round trip optical gain balances the round trip optical loss and lasing starts. With optical loss caused by outcoupling of photons through the mirrors and internal loss due to free carrier absorption, the threshold current (I_{th}) and the threshold optical gain (g_{th}) can be estimated from:

$$I_{th} = \frac{qV_a}{\eta_i} R_{sp}(\Delta n_{th}), \tag{3.2}$$

$$g_{th} = \frac{1}{\Gamma}[\alpha_i + \alpha_m] = \frac{1}{\Gamma}[\alpha_i + \frac{1}{2L}\ln(\frac{1}{R_1 R_2})], \tag{3.3}$$

where q, V_a and η_i are the electron charge, active region volume and internal quantum efficiency, respectively. Δn_{th} is the threshold carrier density. Γ is the optical confinement factor, which defines the overlap between the optical field in the resonator and the active region. α_i is internal optical loss. α_m is the mirror loss represented by the mirror reflectivities R_1 and R_2. In a VCSEL, these are the reflectivities of the two DBRs. Finally, L is the length of the cavity, which in a VCSEL is the spacing between the DBRs plus the effective penetration of the optical field into the two DBRs.

In a VCSEL, due to its vertical geometry and limited thickness of the active region, the round trip optical gain is small. Therefore, highly reflective DBRs (>99% reflectivity) are used to reduce the round trip optical loss. In addition, the active region is positioned at the peak (anti-node) of the optical field between the two DBRs for maximum modal gain. Furthermore, the active region consists of a number of very thin layers, referred to as multiple quantum wells (MQWs), where 1D carrier confinement leads to quantization of the electronic states, which increases optical gain and differential gain through a modification of the density of states. In addition, the QWs are commonly lattice mismatched to introduce strain. Strain leads to further modifications of the density of states and further improvements of gain and differential gain [65]. A high differential gain improves the modulation speed of VCSELs used in datacom systems [66].

3.1.2   Mirrors and resonator

Apart from the requirement of the round-trip optical gain being equal to the round-trip optical loss for lasing to occur, Equation 3.3, the phase of the optical field propagating inside the resonator must repeat itself after one round-trip:

$$exp(-j\frac{2\pi}{\frac{\lambda_0}{n_{eff}}} \cdot 2L) = 1 \rightarrow \lambda_0 = \frac{2Ln_{eff}}{m}, \tag{3.4}$$

where λ_0 is the free space wavelength, n_{eff} is the effective refractive index in the cavity, and m is an integer representing the longitudinal mode number. Equation 3.4 defines a large number of longitudinal modes with different wavelengths. However, only those within the spectral range where gain is provided by the MQWs in the active region can reach lasing.

In a VCSEL, optical feedback and longitudinal (vertical) confinement are provided by the highly reflective top and bottom DBRs, Figure 3.2. The cavity is very short and the effective length of the resonator is small enough for only one longitudinal mode to be within the gain bandwidth of the MQWs. Therefore, the VCSEL is a single longitudinal mode laser.

The DBR is a stack of multiple layers with alternating refractive index. Each layer is a quarter-wavelength thick, which implies that reflections at the interfaces add in phase to generate a high reflectivity over a certain optical bandwidth. Commonly used materials for DBRs used in VCSELs are semiconductors and dielectrics. Semiconductor DBRs are prepared by epitaxial growth techniques while dielectric DBRs are deposited by sputtering with precise deposition rates. The peak reflectivity of a DBR (at the Bragg wavelength) depends on the number of layers pairs and the refractive index contrast, Δn, between the materials used. The spectral width (stopband) depends only on Δn [66]. For instance, a semiconductor DBR with different Al-content AlGaAs layers has a relatively low index contrast (GaAs/Al$_{0.90}$Ga$_{0.10}$As with Δn=0.49 at 1050 nm [67]) and therefore needs 20-30 pairs for sufficient reflectivity, while a dielectric DBR typically requires less than 10 pairs to reach >99% reflectivity (SiO$_2$/TiO$_2$ with Δn=0.9 at 1050 nm [68]). A hybrid DBR, consisting of a lower reflectivity DBR stack covered by a layer of metal, or a high contrast grating (HCG) can also be used to form a mirror with sufficient reflectivity [39].
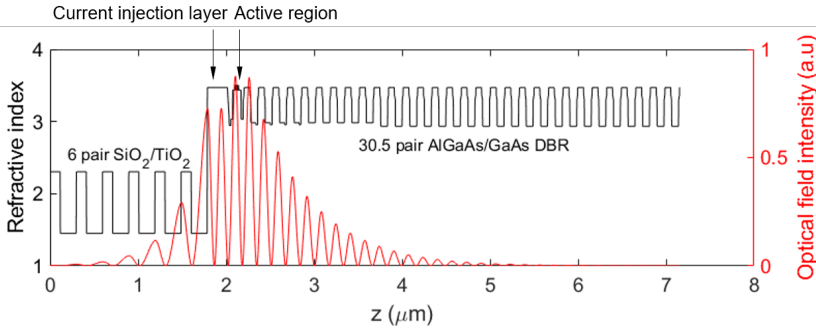
Figure 3.2: Refractive index profile and optical field intensity (standing wave) propagating along the optical axis of a VCSEL with a 30.5 bottom semiconductor DBR and a 6 pair SiO$_2$/TiO$_2$ top DBR.
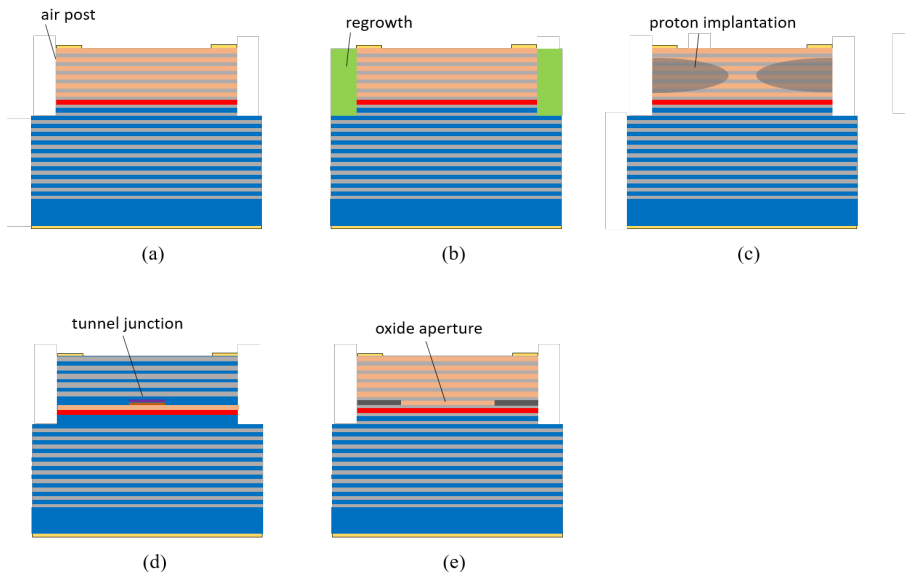
Figure 3.3: Different approaches for transverse optical and current confinement. (a) etched air post, (b) buried heterostructure, (c) ion implantation, (d) buried tunnel junction, and (d) oxide aperture.

In this thesis, the VCSELs in Papers B and C have a semiconductor bottom DBR and a dielectric top DBR, Figure 3.2.

Contrary to an edge-emitting Fabry-Perot laser (Figure 3.1.b), where the emission wavelength is determined by the wavelength of the gain peak, the wavelength of a VCSEL is determined by the resonance wavelength. This leads to a reduced temperature dependence of the emission wavelength, similar to an edge-emitting distributed feedback laser where the wavelength is set by the reflection from the grating.

3.1.3 Transverse current and optical confinement

In a VCSEL, longitudinal confinement of the resonating optical field is provided by the DBRs, see Figure 3.1.a. In addition, the optical field has to be confined in the transverse direction and the current has to be confined to the region where the optical field is confined.

There are several techniques for transverse optical and current confinement, such as etched air post [60], buried heterostructure [69], ion implantation [70], buried tunnel junction (BTJ) [71], and oxide aperture [72], as shown in Figure 3.3. The first VCSELs used an etched air post mesa with transverse optical confinement provided by the refractive index step at the semiconductor-air interface. However, while fabrication is simple the design has several issues in-

cluding large scattering losses from the sidewalls and high thermal resistance. With regrown semi-insulating semiconductor material around the etched mesa (the buried heterostructure approach), thermal resistance and scattering loss are eliminated. However, the regrowth process is challenging. Ion implantation, with protons deeply implanted in the top-DBR, was used for the first commercial VCSEL. The implanted region is electrically isolating and therefore provides transverse current confinement. However, it does not provide the refractive index step needed for transverse optical confinement. Therefore, the modal and beam characteristics of the VCSEL become strongly dependent on current through thermal lensing and spatial hole burning [73]. Furthermore, the fabrication of small aperture VCSELs by this technique is difficult. The BTJ provides both transverse optical and current confinement and has been successfully used for InP-based VCSELs operating at 1.3 and 1.55 μm. It is more difficult to implement in a GaAs-based VCSELs due to higher bandgap, higher resistance tunnel junctions in this material system. GaAs-based VCSELs commonly use a high-Al content layer ($Al_{0.98}Ga_{0.02}As$) positioned in the top-DBR close to the active region. After etching a mesa, this layer is subjected to hot water vapor for selective oxidation to form an oxide aperture. The oxidized layer is electrically isolating and has a lower refractive index than the non-oxidized layer. The oxide aperture therefore provides both current and optical transverse confinement. The strength of the transverse optical confinement depends on the size of the aperture, the thickness of the oxidized layer, and its vertical position relative the longitudinal optical standing wave. Depending on the strength, the VCSEL can support one or multiple transverse modes. Positioning the oxide aperture at a node of the optical field leads to weak optical guiding which facilitates single mode emission. It also reduces scattering loss at the aperture [74].

3.1.4 Optical modes

As discussed earlier, in the oxide-confined VCSEL, see Figure 3.1.a, transverse optical and current confinement is provided by the oxide aperture. The oxide aperture diameter depends on the mesa diameter, the oxidation rate and the oxidation time. A small oxide aperture, and therefore a single transverse mode VCSEL, can be achieved by controlling the required parameters during the wet oxidation process. A larger oxide aperture leads to a multiple transverse mode VCSEL. However, in the vertical direction, the VCSEL cavity is sufficiently short to support only one longitudinal mode within the gain bandwidth of the QWs. Therefore, the VCSEL is inherently single longitudinal mode, while the number of transverse modes is defined by the oxide aperture size. Spectra of a singlemode (SM) and multimode (MM) VCSELs are shown in Figure 3.4. The different transverse modes emit at slightly different wavelengths because of their different effective mode indices. This increases the spectral width of a MM-VCSEL compared to a SM-VCSEL.

To further study the spectral characteristics of the VCSEL (with cylindrical
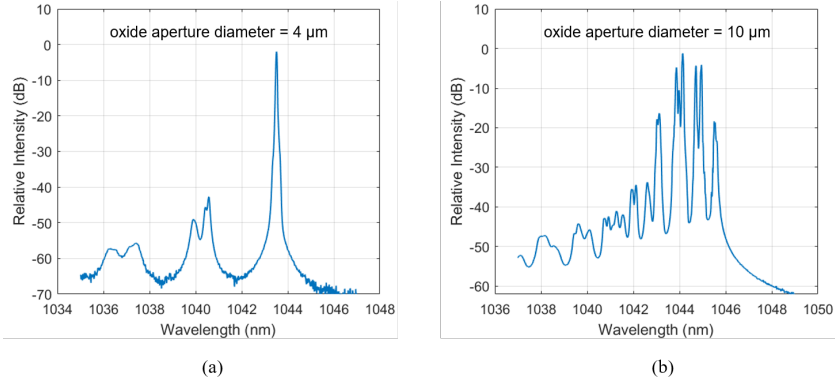
Figure 3.4: Spectrum for a SM-VCSEL with a 4 μm oxide aperture (a) and a MM-VCSEL with a 10 μm oxide aperture (b).

symmetry), one considers a cylindrical step-index waveguide with the index step induced by the low refractive index of the oxidized layer. The cylindrical waveguide has a core diameter equal to the oxide aperture diameter (d_{ox}) and an index step Δn_{eff} equal to the difference in effective index between non-oxidized and oxidized regions. Δn_{eff} is on the order of 0.01 or less depending on thickness and positioning of the oxide aperture. Using the wave equation and the boundary conditions at the core-cladding interface, the transverse modes supported by the VCSEL can be identified. When $\Delta n_{eff} \ll n_{eff}$, where n_{eff} is effective refractive index of the optical mode in the VCSEL resonator, the weakly guiding approximation can be used [75] and the transverse modes can be described in terms of linearly polarized modes, LP_{mn}, where m and n are the
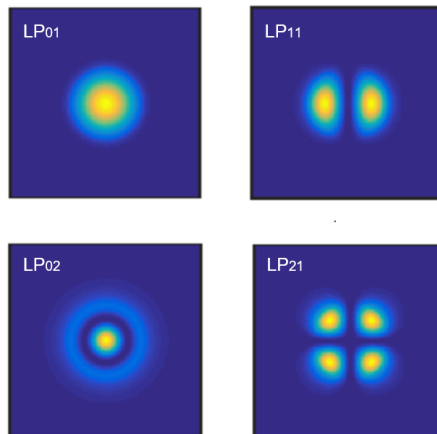
Figure 3.5: Transverse intensity distribution of the lowest order LP_{mn} modes.

azimuthal and radial mode numbers, respectively. In the VCSEL, the lowest order transverse mode (the fundamental mode) is the LP_{01} with a Gaussian transverse intensity distribution, Figure 3.5.

However, under current injection the modal analysis becomes more complex due to the self-heating and presence of carriers in the active region. Self-heating results in thermal lensing which leads to stronger transverse confinement of the optical fields. The presence of carriers in the active region leads to gain guiding [76] and anti-guiding through the plasma effect. Therefore, the number of guided modes varies with current. In addition, spatial hole burning caused by intense stimulated emission in regions with a high photon density leads to mode competition and switching. An accurate analysis of the modal characteristics of a VCSEL and their dependence on current and ambient temperature thus requires a self-consistent treatment that accounts for the built-in index step, gain guiding, carrier anti-guiding and spatial hole burning.

3.1.5   Static performance measures

Of primary importance for the static (DC) performance of a VCSEL is the dependence of output power, voltage and emission spectrum on current. For the current-power-voltage (IPV) measurements, the VCSEL is biased by a DC current source at different currents and its voltage at each current is measured by the DC source and delivered to a multimeter. Emitted light from the VCSEL is collected by a reverse biased large area PD or an integrating sphere and converted to a photocurrent. The PD/sphere must be close enough to the VCSEL to collect all light emitted. For GaAs-based 850-980 nm VCSELs, a Si-based PD is suitable, while a Ge or InGaAs-based is needed at longer wavelengths. The generated photocurrent is measured by a load resistance (50 Ω) connected in parallel to the multimeter. Moreover, a temperature controller sets and controls the VCSEL ambient temperature. If measurements of power along a certain polarization is needed, a polarizer is positioned between the VCSEL and the PD/sphere. In this case, because of the large dimensions of the polarizer, the distance between the VCSEL and the PD/sphere is too long for collecting all the light emitted by the divergent VCSEL beam. Therefore, an anti-reflection (AR) coated lens with sufficient numerical aperture (NA) is placed above the VCSEL to collimate the VCSEL beam.

For spectral measurement, the VCSEL is biased with the same DC source. Here, the VCSEL beam is collected by a butt-coupled bare optical fiber positioned just above the VCSEL and connected to an optical spectrum analyzer (OSA). However, if either the VCSEL aperture is too large or the beam is too divergent, a large NA AR-coated lens package is required to couple the VCSEL beam to the optical fiber with high efficiency.

3.2 Dynamic characteristics and performance measures

Data centers interconnects are dominated by VCSEL-based OIs and their capacity depends on the VCSEL dynamics. To encode data on the light emitted by the VCSEL, its intensity is directly modulated by the current. The VCSEL must be fast enough to react to changes in the current at the data rate considered. Since electron-hole recombination is associated with a certain lifetime (the differential carrier lifetime) and since it takes a certain time for generated photons to escape from the resonator (the photon lifetime), the VCSEL cannot be modulated infinitely fast. Therefore, a proper and intelligent design is needed for a high modulation bandwidth. The dynamic properties of a VCSEL, like any other directly modulated semiconductor laser, are described by the resonant interaction between injected carriers in the active region and photons in the lasing modes of the resonator. This interaction is described by rate equations for the carrier and photon densities [66]:

$$\frac{dN}{dt} = \frac{\eta_i I}{qV_a} - \left(AN + BN^2 + CN^3\right) - v_g G S_m, \tag{3.5}$$

$$\frac{dS_m}{dt} = \Gamma v_g G S_m - \frac{S_m}{\tau_p} + \Gamma \beta B N^2, \tag{3.6}$$

where N is the excess carrier density in the active region and I is the bias current. A, B and C are the Shockley-Read-Hall, the radiative and the Auger recombination coefficients, respectively (Equation 3.1). v_g is the active region group velocity, G the active region optical gain per unit length, S_m the photon density in mode m, τ_p the photon lifetime and β the fraction of the spontaneous emission that adds to the photon density of the modes. The subscript m in Equations 3.5 and 3.6 indicates that for each transverse mode of the VCSEL, a separate rate equation for the photon density is needed. However, in an oxide-confined VCSEL where the transverse optical fields are strongly overlapping, due to the index guiding, a single rate equation for the photon density is sufficient for capturing the most important aspects of VCSEL dynamics [77]. At high photon densities, gain compression due to nonlinear effects such as spectral hole burning and carrier heating [78] occur, and this can be accounted for by a photon density dependent optical gain:

$$G(N, S) = \frac{g(N)}{1 + \epsilon S}, \tag{3.7}$$

where g and ϵ are the uncompressed gain coefficient and gain compression factor, respectively.

Equations 3.5 and 3.6 are coupled differential equations and have to be solved numerically under arbitrary variations of the injection currents. However, under small-signal modulation and using a single rate equation for the

photon density, an analytical solution can be derived which yields a transfer function $H_i(f)$ for the intrinsic small-signal modulation response:

$$H_i(f) = \text{const} \cdot \frac{f_r^2}{f_r^2 - f^2 + j\frac{f}{2\pi}\gamma}, \tag{3.8}$$

with [79]:

$$f_r \approx \frac{1}{2\pi} \sqrt{\frac{v_g g_0 S}{\tau_p (1 + \varepsilon S)}}, \tag{3.9}$$

and:

$$\gamma \approx K f_r^2 + \gamma_0, \quad \text{with} \quad K = 4\pi^2 \left[\tau_p + \frac{\varepsilon}{v_g g_0} \right], \tag{3.10}$$

where f_r is the resonance frequency, γ the damping rate, g_0 the differential gain, γ_0 the damping offset and K is referred to as the K-factor. This shows that the intrinsic response of the VCSEL is that of a second order system and is therefore characterized by a resonance frequency and a damping rate.

The modulation bandwidth, f_{3dB}, is defined as the frequency at which the response is half of its low frequency value. Since damping increases with current, the intrinsic maximum bandwidth of the VCSEL is ruled by the Equation 3.10. A high resonance frequency, favored by a high photon density, a short photon lifetime, and a high differential gain, is still needed for a high modulation bandwidth. The photon density and lifetime are largely controlled by the reflectivity of the DBR through which light is coupled out (usually the top-DBR) and a high differential gain is achieved by strained QWs in the active region. With both resonance frequency and damping rate increasing with current and photon density, and with the damping rate increasing faster ($\gamma \propto S$) than the resonance frequency ($f_r \propto \sqrt{S}$), the maximum intrinsic bandwidth is limited by the K-factor [66]:

$$f_{3dB}^{max} \approx \frac{2\sqrt{2}\pi}{K}. \tag{3.11}$$

The increase of the resonance frequency with current and photon density, Equation 3.9, is quantified by the D-factor:

$$f_r = D \cdot \sqrt{I - I_{th}}, \quad \text{with} \quad D = \frac{1}{2\pi} \sqrt{\frac{\eta_i \Gamma v_g}{q V_a} \cdot g_0}. \tag{3.12}$$

A high resonance frequency is therefore also favored by a small active region volume, as we have in a small aperture VCSEL. The high D-factor achievable with a properly deigned VCSEL translates to a high resonance frequency at a low current, which is important for energy-efficient, high-speed VCSELs.
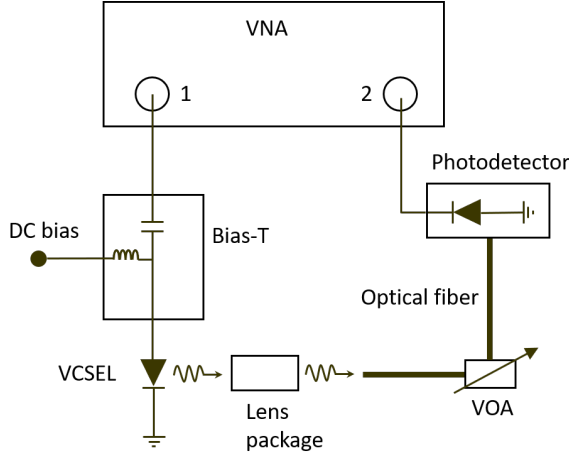
Figure 3.6: Measurement setup for small-signal modulation response.

At high internal VCSEL temperature, caused by a high ambient temperature and/or current-induced self-heating, thermal effects limit the bandwidth by reducing the differential gain and increasing the leakage current from the MQWs (reducing the internal quantum efficiency). Furthermore, at high modulation frequencies, the parasitic capacitance (primarily over the oxide layer) shunts the modulation current past the active region, which also reduces the modulation response. To include the effects of parasitics in the small-signal modulation response, Equation 3.8 is modified as:

$$H_i(f) = \text{const} \cdot \frac{f_r^2}{f_r^2 - f^2 + j\frac{f}{2\pi}\gamma} \cdot \frac{1}{1 + j\frac{f}{f_p}}, \tag{3.13}$$

where f_p is parasitic cut-off frequency. As a result, a VCSEL design with low electrical resistance, low capacitance, low heat generation and low thermal impedance is important for a high modulation bandwidth. The DBR resistance is reduced by graded composition interfaces and modulation doping, or mostly eliminated by an intra-cavity contact design [80]. The parasitic capacitance across the oxide layer can be reduced by introducing extra oxide layers [79, 81]. Lower thermal impedance can be achieved by employing binary alloys in the DBR to the extent possible considering the wavelength [82].

To experimentally determine the dynamic characteristics of a VCSEL (f_r, f_{3dB}^{max}, γ, f_p and their dependence on current), the small-signal modulation response (S_{21}) is measured and the transfer function in Equation 3.13 is fitted to the measured response. Subsequently, the D- and K-factors can be extracted. S_{21} is measured using the setup shown in Figure 3.6. A small sinusoidal modulation current, generated by a vector network analyzer (VNA), is superimposed on the bias current through a bias-T and applied to the VCSEL using a high

frequency RF probe. The VCSEL beam is coupled to a tilted MMF through an AR coated lens package. A variable optical attenuator (VOA) connects the MMF to a high-speed PD with the output connected to the VNA. The VOA is used to avoid saturating the PD. Before the fitting, the VCSEL frequency response is de-embedded from the measured response by accounting for the frequency dependent insertion loss of the RF probe and PD frequency response.

For the large signal modulation response, which is what is relevant for a VCSEL used in a datacom link, a pseudo-random data signal is generated by a pattern generator according to the desired modulation format and fed to the VCSEL through the bias-T. After detection of the optical signal generated by the VCSEL by an optical receiver, the received signal is analyzed using eye-diagrams and an error detector. The eye diagram reveals the transient dynamics, including rise- and fall-times and whether excessive overshoot and ringing causes timing jitter and inter-symbol interference due to an insufficient damping of the modulation response. The error detector is used to determine the bit-error-ratio (BER), which is a measure of the probability that data bits are incorrectly decoded.

Chapter 4

Monolithic multi-wavelength VCSEL arrays

The VCSEL is the dominating light source for short-reach OIs because of its superior cost and power efficiency [18]. Today, higher speed VCSELs [83] are commercialized, which together with higher order modulation formats [84] enable lane rates beyond 100 Gbit/s [23]. Multiple (parallel) fibers provide an aggregate capacity of more than 400 Gbit/s [18]. Further improvements of the aggregate capacity can be achieved using multiple cores per fiber (SDM) [65] or multiple wavelengths per fiber (WDM) [27]. This allows for scaling the capacity of VCSEL-based OIs much beyond 1 Tbit/s [28].

As described in Section 2.2, a WDM based transceiver, known as SWDM4, with four-channel coarse WDM (CWDM) and 30 nm channel spacing (850, 880, 910, 940 nm) enables up to 400 Gbit/s (4 × 100 Gbit/s) single fiber capacity [26,27]. In such transceivers, the VCSEL are discrete, rather than being monolithic multi-wavelength arrays, since they are fabricated from different epitaxial wafers. This leads to a large footprint. With an increasing number of wavelengths, the footprint will be even larger, which becomes increasingly problematic for applications requiring small footprint and high bandwidth density, such as transceivers for co-packaged optics [85].

Monolithic multi-wavelength VCSEL arrays with densely spaced VCSELs lead to a smaller footprint and higher bandwidth density. However, in such arrays, the number of channels and the channel spacing are limited by the optical gain bandwidth of the active region in the VCSEL. On the other hand, a channel spacing sufficiently large is needed to accommodate for wavelength drift with temperature. For GaAs-based VCSELs at ~ 1 μm, with a drift of ~ 0.1 nm/°C and considering for the limited gain bandwidth, arrays of 4 to 8 channels with a corresponding spacing of 8 to 4 nm, depending on the temperature range, seems reasonable for uniform performance over the array.

A small footprint and a high bandwidth density also require a compact

integration platform for multiplexing and fiber coupling. While SOI waveguides absorb at the short wavelengths of GaAs-based VCSELs, SiN waveguides on Si are transparent, while also being CMOS compatible [86]. Therefore, a SiN PIC on Si, with low loss waveguides, MUXs and tapered fiber couplers [87], is a suitable integration platform (Figure 2.2).

In addition to being high-speed, there are three main requirements on the VCSELs in a monolithic multi-wavelength VCSEL array for use in a CWDM transmitter. Each VCSEL has to be single transverse mode and linearly polarized because of the GC used to couple the light from the VCSEL to the SiN waveguide and because the SiN waveguide is a SM waveguide. Moreover, the wavelengths of the VCSELs in the array need to be precisely set with a specific channel spacing. In this work, the intra-cavity phase tuning technique is used to set the wavelengths. Intra-cavity phase tuning is a technique where the cavity length, and therefore the emission wavelength, of a VCSEL with an epitaxial bottom-DBR, active region and current injection layer is modified before the deposition of a dielectric top-DBR. The cavity length can be changed by thinning either the semiconductor current injection layer above the active region [46] or an additional dielectric layer above the current injection layer [45] before top-DBR deposition. While intra-cavity phase tuning is most effective in controlling the resonance wavelength, it requires precise etching or deposition for accurate wavelength control. To achieve the required linearly polarized single transverse mode, the integration of a transverse and polarization mode filter on the surface of an 850 nm VCSEL with a semiconductor top-DBR has been explored.

4.1 Wavelength setting

In a CWDM transceiver, the wavelength of each VCSEL in the array and the spacing between the wavelengths (the channel spacing) have to be precisely set. In this work (Papers A, B and C), intra-cavity phase tuning by thinning of the current injection layer before the top dielectric DBR deposition has been used for wavelength setting. An Ar-ion-beam etching (Ar-milling) process was used to thin the current injection layer. Ar-ion-beam etching is a pure physical etch process (Ar is a noble gas with very low chemical reactivity) with slow etch rate (~ 3 nm/min with 3 mA beam current) and provides sub-nanometer precision in etch depth. As a result, the cavity becomes shorter and consequently the resonance wavelength is blue-shifted, at a rate of ~ 0.95 nm/nm for the VCSELs used here. In addition, Ar milling must not introduce additional roughness in the etched area. This is essential for high performance VCSELs since a rough surface would cause optical scattering loss, which would degrade performance (increase the threshold current and reduce the slope efficiency) because of the high optical field intensity at the semiconductor-dielectric interface close to the center of the resonator. Surface scanning of etched and unetched areas using atomic force microscopy (AFM) revealed that the etched area is as smooth as

the unetched, see paper A.

To form the full cavity (bottom semiconductor DBR + semiconductor active region + top dielectric DBR), 6 pairs of SiO_2/TiO_2 with quarter-wavelength thickness were sputtered on the etched surface. Deviations in thickness from a quarter-wavelength (ideally 182 and 116 nm, respectively, at the center wavelength of 1055 nm) lead to a change in the reflection phase and therefore in the resonance wavelength. Errors in the first dielectric DBR pair have the largest impact, while errors in pairs further away from the cavity have less impact. For instance, a 5 nm error in the first pair layers shifts the resonance wavelength by 1.4 nm, while the same error in the second pair shifts by only 0.6 nm. The thickness of the topmost layer (TiO_2) is also important. While it has the least impact on the resonance wavelength, it affects other parameters, like the photon lifetime and therefore threshold current, slope efficiency and modulation speed, due to the high refractive index step at the TiO_2-air interface. To minimize errors in the dielectric DBR layers, measurements of the thickness and refractive index of each layer are required. This was done by depositing the layers individually on an adjacent Si wafer and measuring the required parameters by ellipsometry before depositing the next layer. If more material was needed, it could be deposited to achieve the correct thickness.

The choice of wavelengths (1040-1070 nm) is motivated by the opportunities for 1) developing even high-speed singlemode VCSELs at these wavelengths, 2) longer transmission distance since both fiber chromatic dispersion and attenuation is lower than at 850 nm [88], 3) multiplexing in a SiN PIC on Si with flip-chip integrated multi-wavelength VCSEL arrays [49], and 4) lower-voltage multi-channel drivers to form compact and energy-efficient high-capacity CWDM transmitters.

4.2 Array uniformity

Uniformity limitations of monolithic multi-wavelength VCSEL arrays, in terms of static and dynamic performance, are discussed in this section. Uniformity of static performance requires uniformity of threshold current and slope efficiency, while uniformity of the dynamic performance is quantified by the uniformity of resonance frequency, maximum bandwidth, damping rate, and parasitic cut-off frequency.

In a monolithic multi-wavelength VCSEL array with wavelengths set by intra-cavity phase tuning, uniform performance in terms of threshold current and slope efficiency over a certain wavelength range requires careful consideration of the spectral dependence of three parameters. These are the DBR reflectances, the optical confinement factor, and the optical gain in the QWs, which control the variation of cavity loss and modal gain with wavelength. Critical balancing of these dependencies is needed for uniformity in terms of e.g., threshold current and slope efficiency. Thinning the phase tuning layer not only shifts the wavelength, but also moves the optical standing wave and there-

fore the overlap with the QWs (the confinement factor) becomes wavelength dependent. Small variations of slope efficiency can be achieved by spectral matching of the DBR reflectances. This is accomplished by spectrally aligning of the bottom-DBR (with narrower bandwidth) with the highest reflectance region of the top-DBR (with wider bandwidth), see Figure 4 in Paper B. In case of any misalignment, the slope efficiency drops and the threshold current increases. Small variations of the threshold current require small variations of the threshold carrier density, Equation 3.2. This can be achieved by proper spectral alignment where the wavelength dependence of threshold gain balances the wavelength dependence of optical gain, resulting in small variations of threshold current over wavelength, see Paper B.

The dynamic performance of a VCSEL is described by several parameters, including most importantly the D- and K-factors and the parasitic pole frequency. In a monolithic multi-wavelength VCSEL array fabricated by the intra-cavity phase tuning technique, the wavelength dependence of these parameters determines the wavelength dependence of the modulation response and the associated bandwidth and damping characteristics. Because the VCSEL array is monolithic, and assuming all VCSELs have the same aperture size, the electrical resistance and capacitance should be the same for all VCSELs. This implies that the parasitic pole frequency should be the same. With good uniformity of threshold current and slope efficiency, the output power and photon density at a certain current should also be similar among the VCSELs in the array. Furthermore, the nearly equal DBR reflectances and cavity lengths implies that the photon lifetimes and the optical confinement factors are nearly the same (see Paper B). The remaining parameter of importance for the D- and K-factors (Equations 3.10 and 3.12), and therefore the modulation response and the damping characteristics, is the differential gain. The differential gain, which is larger on the short wavelength side of the gain peak than on the long wavelength side (see Paper B, Figure 7) and therefore increases when the wavelength is reduced, is more wavelength dependent than all other parameters. It is therefore expected that the D-factor, and therefore the resonance frequency, is higher at short wavelengths (Equation 3.12) and that the K-factor, and therefore the damping rate, is lower at short wavelengths. To confirm this, the modulation response (S_{21}) of the single-mode VCSELs in Paper B was measured using the setup shown in Figure 3.6 and the transfer function in Equation 3.13 was fitted to the measured response to extract the D- and K-factors. The results shown in Table 4.1 confirm the expected dependencies. To what extent these variations affect the variation of modulation bandwidth and damping with wavelength depends on to what extent the modulation response is limited by parasitics and the intrinsic response.

Table 4.1: *D*- and *K*-factors extracted from the measured modulation response for the different wavelength single-mode VCSELs in Paper B.

$\lambda(nm)$	D (GHz/$\sqrt{mA}$)	K (ns)
1066.9	6.951	0.30
1059.7	7.851	0.203
1052.2	10.195	0.179
1043.2	11.531	0.196

4.3 Transverse and Polarization Mode Control

The use of an integrated transverse and polarization mode filter for selecting the fundamental transverse mode and pinning the polarization was explored with a full semiconductor VCSEL at 850 nm (Paper D). The VCSEL is a GaAs-based oxide-confined VCSEL with a relatively large oxide aperture (5 µm). The large aperture reduces the electrical resistance, which increases the output power through reduced self-heating. However, the large aperture supports multiple transverse modes and the polarization of these modes is not controlled because of the circular symmetry of the VCSEL.

To control the polarization and select the fundamental mode, a transverse and polarization mode filter is used (Paper D). The mode filter is a sub-wavelength grating etched in an area with a diameter less than the diameter of the oxide aperture (3 μm), see Figure 4.1. Before etching, the topmost layer optical thickness is a half wavelength and therefore acts as an anti-phase reflector for all modes. After mode filter etching, the optical thickness is reduced to a quarter wavelength in the etched area and the layer then acts as a spatially selective in-phase reflector. Therefore, its spatial extent controls the transverse mode selectivity [89]. The sub-wavelength grating creates as a polarization dependent effective index medium. Therefore, the effective index for parallel and perpendicular polarized light to the grating lines is different and results in

(a)   (b)
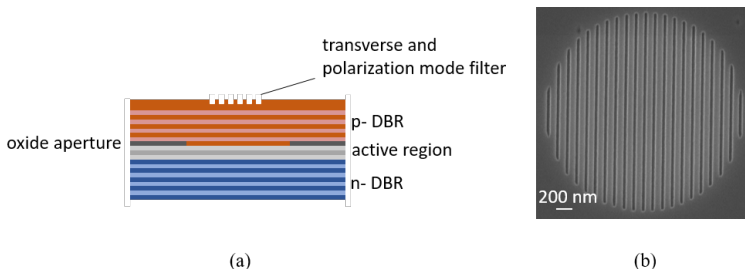
Figure 4.1: (a) An oxide-confined VCSEL with a sub-wavelength grating mode filter etched into the surface. (b) Top view of the mode filter.

anti-phase and in-phase reflection, respectively [89]. Thus, the spatial extent of the filter controls the transverse mode selectivity while the orientation of the grating lines provides polarization mode selectivity. The sub-wavelength grating pitch, in contrast to a pitch larger than the wavelength, also avoids excessive optical loss and beam degradation due to diffraction. A record high output power of 6 mW was achieved with >30 dB suppression of higher order transverse modes and >20 dB suppression of the orthogonal polarization mode.

While this technique has been successfully explored for 850 nm VCSELs with a top semiconductor DBR, the technique should also be applicable to ~ 1 μm VCSELs with a dielectric DBR. However, this remains to be proved.

Chapter 5

VCSEL integration on silicon photonic integrated circuits

Over the past decade, SiP has attracted increasing attention and vast resources have been invested in the development of PICs [90]. At the core of these efforts is the opportunity to merge optical and electrical circuits on Si [91–93]. Ideally, all components should be CMOS compatible. Being CMOS compatible implies the use of established CMOS fabrication processes also for the photonic components. The CMOS technology allows for high-volume and high-yield production, which reduces the cost of manufacturing. Both SOI for wavelengths $> \sim 1 \ \mu$m and SiN-on-silicon for wavelengths also in the very-near-infrared and the visible, enable PICs with low loss and small footprint. Many of the key components, e.g., low loss waveguides, MUXs, DEMUXs, and couplers are readily available on both platforms [94] and are used in many applications, e.g., optical communication [95], sensing [96] and spectroscopy [97].

5.1 Integration techniques

The remaining obstacle to achieve fully functional SiP PICs is the lack of an ideal on-chip light source. The problem originates from the fact that Si is an indirect bandgap material and therefore cannot efficiently emit or amplify light. Although there are efforts to epitaxially grow CMOS compatible direct bandgap material on Si, e.g., Ge-based [98], most efforts involve the use of direct bandgap III-V materials for efficient light amplification and generation.

There are several techniques for light source integration on SiP PICs, including monolithic, heterogeneous and hybrid [91]. Monolithic integration of III-V lasers on Si, where the III-V material is epitaxially grown on the Si substrate, may be the ultimate goal to unlock the full potential of SiP PICs with dense integration of efficient light sources. For instance, for high-capacity on-chip interconnects, more than 1000 optical channels may be required to achieve

a total bandwidth of ~ 10 Tbit/s with high efficiency [99]. On the other hand, the growth of III-V semiconductors on Si is challenging. This is because of the large mismatch in lattice constant between the III-V semiconductors and Si, e.g., 8% for InP on Si and 4% for GaAs on Si, which results in dislocations and degradation of laser performance. Therefore, other integration approaches are explored [98–100].

In heterogenous integration, epitaxial III-V films are bonded to the Si-PIC by either direct or adhesive bonding [101]. This is followed by post-processing to create an on-PIC laser. In direct bonding, the films are bonded without any intermediate layer at high temperature using intermolecular forces, e.g., Van der Waals forces and covalent bonds. The bonding requires smooth, clean, and flat surfaces [102]. Adhesive bonding is more forgiving in terms of surface roughness and contaminations and is therefore the preferred technique in many cases. Examples of bonding agents are SU-8 and benzocyclobutene (BCB). Adhesive bonding is done at a lower temperature than direct bonding, and the quality of bonding depends on parameters like adhesion material and thickness, temperature and the pressure applied [103]. While heterogeneous integration is a promising approach to III-V light source integration on Si, it is not strictly CMOS compatibility, but rather a back-end process.

Hybrid integration is based on opto-mechanical mounting of pre-fabricated devices on the Si-PIC by pick-and-place techniques. This includes flip-chip integration [49], transfer printing [104], butt- or edge-coupling [105] and micro-optical-bench (MOB) integration [106], or a combination of these methods. For butt-coupling, the light source is aligned to a waveguide facet of the PIC with critical alignment tolerances. Contrary to butt-coupling, flip-chip integration, transfer printing, and MOB integration use a GC to launch the light into the Si-PIC. The MOB contains not only the light source but also micro-optical elements for beam collimation and redirection. However, the MOB has a relatively large footprint [49]. Transfer printing involves pick-up of pre-processed device coupons from a source wafer and subsequent printing on the target PIC wafer using a stamp. This approach allows for simultaneous printing of a large number of coupons, which improves the production throughput and reduces cost. Flip-chip integration creates a mechanical and electrical bond between the light source and the PIC by soldering. The next section of this chapter introduces flip-chip integration of VCSELs, which is the integration approach explored in this thesis (Paper E).

5.2 VCSEL flip-chip integration

The unique characteristics of VCSELs, including surface-normal emission, low power consumption, and small footprint (smaller than most other light sources), make the VCSEL an interesting light source for flip-chip integration over a GC [49,107–109]. A flip-chip integrated VCSEL occupies an area about an order of magnitude smaller than a typical MOB. Moreover, with flip-chip integration,

the performance of the VCSEL can be independently optimized and tailored for the specific requirements set by the PIC and the application. With the GC being sensitive to polarization and the Si or SiN waveguide being SM, for high coupling efficiency the VCSEL must be SM and properly polarized with respect to the grating lines. Both of these requirements are met by the VCSEL presented in Paper D, which also provides the high optical power needed to cope with the optical losses in the PIC. However, SM-VCSELs are sensitive to optical feedback [110] and therefore optical back-reflection to the VCSEL must be avoided. In addition, most applications require uni-directional coupling to the waveguide. Both requirements can be met by flip-chip integration at an angle with respect to the surface of the GC. Flip-chip integration of a VCSEL on a SiN PIC is illustrated in Figure 2.3. For a specific GC, coupling efficiency and optical feedback depend on the VCSEL die size and flip-chip angle, and whether the coupling is co-directional or contra-directional. In Paper E, a numerical study using finite-difference time-domain (FDTD) simulations for investigating the dependence of coupling efficiency and optical feedback on flip-chip angle and VCSEL die size is presented. For the numerical study, a simple GC design with straight grating lines and uniform pitch was used to examine general trends and dependencies. Paper E also presents results from experimental work where the VCSEL in Paper D was used for flip-chip integration over a GC on a SiN PIC. Here, a more advanced GC design for higher coupling efficiency was used.

One potential application of VCSEL flip-chip integration on a Si-PIC is for co-packaged optics in datacom transceivers (Figure 2.2). By flip-chip integration of monolithic multi-wavelength VCSEL arrays (Paper B) on a SiN PIC for multiplexing and fiber coupling, a compact and energy-efficient transmitter module for high-capacity wavelength-multiplexed OIs can potentially be built [87].

5.3   On-PIC VCSEL-to-photodetector optical link

Paper E presents a unique on-PIC VCSEL-to- PD optical link, with flip-chip integrated VCSELs and PDs. A schematic of the optical link is shown in Figure 5.1.a. At the input, a VCSEL is flip-chip integrated at an angle over a GC, which couples the VCSEL beam to a SM SiN waveguide. At the output, a GC couples the light from the waveguide to a flip-chip integrated PD. The PD integration angle is 0°. The PD converts the output light to a photocurrent. A microscopic image of the on-PIC VCSEL-to-PD optical link is shown in Figure 5.1.b. Flip-chip integration of the VCSEL and PD requires high accuracies in positioning over the GCs as well as high accuracy in the VCSEL angle. Otherwise, the insertion loss, which is primarily controlled by the GC coupling efficiencies, will increase. The 850 nm VCSEL presented Paper D, with an integrated transverse and polarization mode filter, is used for flip-chip integration over the input GC. The target integration angle is 11° and the GC

(a)   (b)
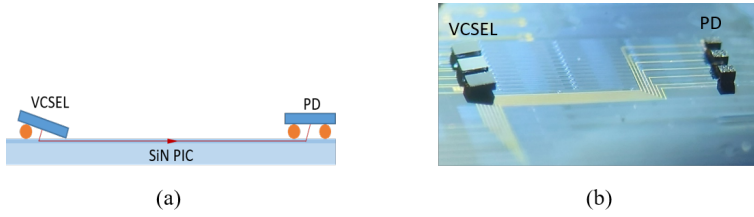
Figure 5.1: On-PIC VCSEL-to-PD optical link with contra-directional coupling at the input and co-directional coupling at the output. (a) schematic illustration and (b) microscope image.

is a dual-etched GC with constant grating period and straight lines. The input GC is connected to a SM SiN waveguide through a tapered section for adiabatic coupling. The SiN waveguide core is sandwiched by SiO_2 cladding layers. At the output, another tapered section connects the waveguide to the output GC. The output GC is a single-etched grating with constant period and straight lines. Top and side view schematics of the SiN-PIC are shown in Figure 5.2. The input GC with a 480 nm grating period provides contra-directional coupling, while the output GC with 580 nm grating period provides co-directional coupling, both at 11°. The output light is collected by a GaAs-based PD with a 20 μm diameter optical aperture and responsivity of 0.4 A/W at 850 nm. The PD is from the VI Systems (D20-850C) and the SiN-PIC is fabricated on the imec BioPIX300 platform [111]. An insertion loss of 20.1 dB was been mea-
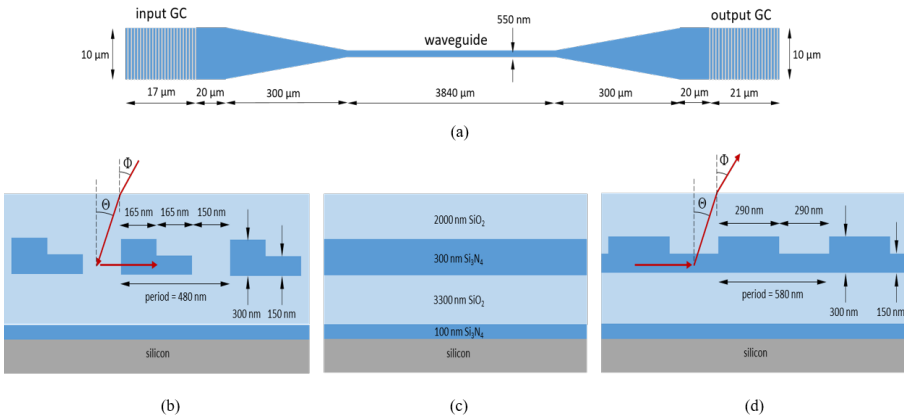
Figure 5.2: (a) PIC top view showing the input and output GCs, the SM waveguide, and the tapered waveguide sections connecting the GCs to the SM waveguide. Cross-sections of the input GC (contra-directional), the SM waveguide, and the output GC (co-directional) along the propagation direction are shown in (b), (c), and (d), respectively.

sured for the VCSEL-PD optical link. Significant improvements are expected with optimized GC designs.

Chapter 6

VCSEL fabrication

The epitaxial VCSEL structures used in this work were grown using the metal-organic chemical-vapor deposition (MOCVD) and provided by IQE Europe Ltd and Jenoptik Optical Systems GmbH. MOCVD provides a good compromise between growth rate and control of layer thickness, composition, and doping. III-metals (Al, Ga, In) are transported into a reactor using gaseous organic compounds. They react with arsine (AsH_3) and adsorb on the heated substrate to form III-As epitaxial films. Introducing Si or carbon to the reactor results in n-type and p-type doping, respectively. After epitaxial growth, several processing steps are needed for the work presented in this thesis. In this chapter, some of the critical steps for the fabrication of multi-wavelength VCSEL arrays and VCSELs with an integrated transverse and polarization mode filter are discussed.

6.1 Metallization and selective oxidation

To be able to inject or extract current to and from any optoelectronic device with low resistance, ohmic contacts are needed. Thin metal films are usually deposited by electron beam evaporation, in which metal vapors are generated when a high-energy electron beam hits the metal source and are deposited on the sample. The deposition rate is accurately controlled by monitoring the mechanical resonance frequency of a crystal. The resonance frequency decreases with increasing film thickness. This evaporation technique was used to deposit Ti/Pt/Au p-contacts and Ni/Ge/Au n-contacts. Depositing the p-contact on a highly p-doped GaAs layer results in an ohmic contact with low resistivity. On the other hand, the n-contact deposited on highly n-doped GaAs requires annealing at 380°C for 1 minute for ohmic behavior with low resistivity.

In an oxide-confined VCSEL, the oxide aperture is formed by selective wet oxidation of a high-Al content AlGaAs layer by subjecting the etched mesa sidewall to hot water vapor at 420°C. A nitrogen bubbler is used to carry water

vapor from a water container held at 95-97°C to the oxidation furnace. Using an array of infrared light emitting diodes (LEDs) and a microscope with a charge coupled device (CCD) camera enable in-situ observation of the wet oxidation. The oxide aperture can be distinguished by the difference in reflectivity between oxidized and non-oxidized areas. The oxidation rate is highly dependent on the furnace temperature and the Al concentration with even a small temperature gradient across the sample leading to large differences in oxidation rate. Since our furnace temperature is not uniform, the chip was turned 180 degrees half-way through the oxidation to improve uniformity. The oxidation rate for $Al_{0.98}Ga_{0.02}As$ is approximately 0.3 μm/min, and roughly twice faster than for $Al_{0.96}Ga_{0.04}As$.

6.2 Etching for intra-cavity phase tuning

Etching of semiconductors can be done using wet or dry etching. The most suitable technique depends on requirements of etch rate, selectivity, and anisotropy. Wet etching is intrinsically chemical and anisotropic. For GaAs, wet etchants contain an oxidizer like H_2O_2 to oxidize the GaAs surface and an acid that dissolves the oxide. Since the etch rate of wet etching depends on the material composition and doping level, and with the etching being more isotropic, in this work dry etching with ions generated in a plasma and accelerated towards the sample by an electric field was used for the intra-cavity phase tuning. The incident ions can be neutral or reactive for pure physical (sputtering) or chemical etching, or a combination thereof. Since a precise, stable, and reproducible etch rate, independent of material composition and doping, was needed we used pure physical etching with neutral ions.

The technique used is Ar-ion-beam etching in an Oxford Ionfab 300 Plus system equipped with an electron emitter for neutralizing the ion-beam and a rotating sample holder for uniform etching over large areas. The etch rate depends on the applied electric field (ion kinetic energy) and the ion beam current (ion density). In this work, the beam current was set to a low value of 3 mA while the Ar flow rate for both the beam and the neutralizer was set to 4 sccm. The voltage controlling the electric field was set to a low value of 300 V. The sample, which was rotated at 3 rpm during etching, was patterned with photoresist (positive photoresist AZ 1512) to enable measurements of etch depth using AFM. An AFM tool (SPM-Bruker Dimension 1300) was also used for measurements of surface roughness.

6.3 Dielectric DBR deposition

In this work, the dielectric DBR was deposited using a sputtering technique. In sputtering, energetic atoms, Ar in this case, are generated in plasma and bombard a target. The Ar ion energy is high enough to overcome the binding

energy of the target particles. As a result, these particles are sputtered away from the target and coat the surface of the sample. For conducting targets, DC sputtering is used where the target has a DC bias. Therefore, there is no accumulation of charge on the surface of the target. For insulating targets, RF sputtering is used.

Reactive sputtering is used when thin films of compound materials are required. In reactive sputtering, a reactive gas is injected to the chamber and reacts with the particles of the target and form the thin film. The sputtering tool used in this work was an FHR MS 150. O_2 was used as the reactive gas to deposit SiO_2 and TiO_2. The O_2 flow was set to 15 sscm for SiO_2 and 4 sccm for TiO_2 and the Ar flow was set to 40 sccm for both films. Six pairs of SiO_2/TiO_2 were deposited one by one to build the dielectric DBR. The thickness of each film was controlled by the deposition time. To minimize the errors in optical thickness, the physical thickness and refractive index of each layer were measured by ellipsometry before the deposition of the next layer. This was done by also depositing the layer on an adjacent Si wafer. If needed, additional material was deposited to reach the correct thickness.

6.4 Mode filter integration

The sub-wavelength grating mode filter was defined as the first step in the fabrication. Since the mode filter should be exactly at the center of the oxide aperture, electron beam lithography and metal alignment marks were used. The same alignment marks were also used to define the VCSEL mesa by electron beam lithography. Therefore, the mode filter and the oxide aperture were perfectly aligned. Dry etching was used to etch the grating into the top GaAs layer. Although a combination of reactive etching and physical sputtering could be used to form the sub-wavelength grating, Ar ion-milling was used for pure physical etching. Ar ion-milling provides the precise control of etch depth needed for the sub-wavelength grating.

Chapter 7

Outlook and future directions

The project ultimately aimed at demonstrating a monolithic multi-wavelength array of high-speed VCSELs in the wavelength range ~1030-1070 nm, with each VCSEL being SM and linearly polarized, and the flip-chip integration of this array on a SiN waveguide platform for multiplexing and fiber coupling. In terms of the VCSEL array, this requires a technique for precise wavelength setting of individual VCSELs in the array, a technique for transverse and polarization mode control, and a high-speed VCSEL design. In terms of the SiP platform, this requires grating couplers with high coupling efficiency, low loss SiN waveguides, a low loss MUX, and a low loss fiber coupler. In addition, flip chip integration requires high accuracy in VCSEL positioning and angle.

Intra-cavity phase tuning was shown to enable the precision in wavelength setting needed (Paper A). Next, the technique was used to demonstrate monolithic 4-channel multi-wavelength VCSEL arrays with precisely controlled wavelengths and channel spacing (8 ± 1 nm) and with a small variation of threshold current and slope efficiency across the channels (Papers B and C). However, there is room for improvements, as shown in Paper B, a slight blue-shift of the wavelengths would improve the balancing of all spectral dependencies for even greater uniformity of threshold current and slope efficiency across the array. With the wavelength of individual VCSELs being controlled by not only the precision of the intra-cavity phase tuning process, but also by the precision in thickness and composition of the layers in the epitaxial semiconductor part, we conclude that the fabrication of multi-wavelength VCSEL arrays on full 4" or 6" wafers with high yield is challenging, even with state-of-the-art equipment for epitaxial growth, etching, and deposition.

The VCSELs in the first generation of monolithic multi-wavelength VCSEL arrays are not high-speed and lack the transverse and polarization mode filter needed for single transverse and polarization mode emission at high optical power. Linearly polarized SM-VCSELs are needed for efficient coupling to the SiN waveguides. Therefore, the mode filter technique developed and successfully demonstrated for 850 nm VCSELs with a semiconductor top-DBR

(Paper D) should be transferred to the VCSELs with a top dielectric DBR in the multi-wavelength VCSEL array. In the full semiconductor VCSELs with a top semiconductor DBR, the mode filter etching is done as the first step. However, with the dielectric top-DBR, this step has to be implemented later in the process flow (after intra-cavity phase tuning and dielectric DBR deposition). Another possibility is to use an intra-cavity mode filter. Here, mode filter integration can possibly be part of the phase tuning process, i.e., the use of one shallow structure for simultaneous wavelength setting, transverse mode selection and polarization mode selection, before dielectric DBR deposition.

Each VCSEL in the array should also be able to operate at a baud-rate of at least 25 Gbaud, for a 25 Gbit/s NRZ or 50 Gbit/s PAM-4 data rate. This requires a high-speed design. Therefore, in addition to having a large intrinsic modulation bandwidth (high differential gain and optimum photon lifetime), the VCSELs should have low resistance, low capacitance, and low thermal impedance. The resistance of the VCSELs in the present multi-wavelength VCSEL arrays, although having an intra-cavity contact, is too high and needs to be reduced. They also have too high capacitance for high-speed modulation. This comes from the lack of a thick low-dielectric constant layer under the p-bond pad. Therefore, a BCB process should be implemented in the next generation.

Apart from the VCSELs, the SiN-PIC used initially for investigating the dependence of coupling efficiency on position and angle accuracy of the flip-chip integration process, and intended for multiplexing and fiber coupling in the future, can be re-designed for lower insertion loss. The input and output grating couplers used in Paper E have high coupling loss, about ∼9 dB each. However, with more advanced GC designs, such as an apodized grating with curved grating lines for improved mode matching and/or a DBR below the waveguide to redirect light transmitted through the GC, the coupling loss can be reduced to ∼2 dB.

Chapter 8

Summary of papers

PAPER A

This paper presents a technique for precise setting of the resonance wavelength of VCSEL micro-resonators in a post-growth fabrication process. An accuracy of ± 2 nm in the wavelength range 1040-1070 nm is achieved by intra-phase tuning using precise and stable Ar ion-beam etching. The precision in etching (± 1 nm) limits the accuracy in wavelength setting to ± 1 nm. The difference is caused by errors in the optical thickness (physical thickness and refractive index) of the dielectric layers used in the top-DBR and by the inherent non-uniformity of the epitaxial layer thicknesses. The technique is developed for the fabrication of monolithic multi-wavelength VCSEL arrays.

My contribution: I did all the fabrication, performed all measurements, and analyzed the results. I wrote the paper and presented the work at the 21st International Vacuum Congress (IVC), 2019 (Malmö, Sweden).

PAPER B

"VCSEL wavelength setting by intra-cavity phase tuning–numerical analysis and experimental verification", *IEEE Journal of Quantum Electronics*, vol. 57, no. 6, 2400307, Dec. 2021. DOI: 10.1109/JQE.2021.3119104

Monolithic multi-wavelength VCSEL arrays, with wavelengths of individual VCSELs precisely set in a post-epitaxial growth process is presented in this paper. A numerical study of the requirements of spectral matching and balancing of DBR reflectances, optical confinement factor, and optical gain for uniformity of threshold current and slope efficiency over wavelength with wavelength set by intra-cavity phase tuning is performed. The requirements are verified by an experimental demonstration of intra-cavity phase tuned VCSELs in the spectral range 1043-1067 nm with a wavelength spacing of 8 ±1 nm enabled by precise Ar-ion-beam etching. Small variations of threshold current and slope efficiency are achieved by close to ideal spectral matching and balancing.

My contribution: I did all the fabrication, performed all measurements, did data analysis, and wrote the paper.

PAPER C

"Monolithic multi-wavelength VCSEL arrays with uniform performance by intra-cavity phase tuning", *27th IEEE International Semiconductor Laser Conference (ISLC)*, Potsdam, Germany, Oct. 10-14, 2021.

Singlemode and multimode monolithic multi-wavelength VCSEL arrays, with wavelengths of individual VCSELs precisely set in a post-epitaxial growth process is studied in this paper. Measurements indicate that VCSELs wavelength and channel spacings are precisely set, 8 ± 1 nm, over the spectral range. For both singlemode (4 μm oxide aperture) and multimode (10 μm oxide aperture) VCSELs, there is an excellent uniformity in terms of threshold current and slope efficiency. Moreover, it was found that the resonance wavelengths red-shift by only $\sim$1 nm when the oxide aperture diameter increases from 4 to 10 μm.

My contribution: I performed all the fabrication and all measurements. I analyzed the results, wrote the paper and presented the work at the 27th IEEE International Semiconductor Laser Conference (ISLC), 2021 (Potsdam, Germany).

PAPER D

"High-power single transverse and polarization mode VCSEL for silicon photonics integration", *Optics Express*, vol. 27, no. 13, pp. 18892-18899, Jun. 2019. DOI:101364/OE.27.018892.

In this paper, a sub-wavelength grating mode filter was etched into the surface of an 850 nm VCSEL for selecting the fundamental transverse mode and pinning the polarization. A single transverse and polarization mode VCSEL with a record output power of 6.5 mW, >30 dB suppression of higher order transverse modes, >20 dB suppression of the orthogonal polarization mode, and narrow beam divergence of 10° (FWHM) is demonstrated. The VCSEL has the modal properties and output power required for light source integration on a silicon photonic integrated circuit.

My contribution: I performed all measurements and data analysis. I co-authored the paper.

PAPER E

"Angled flip-chip integration of VCSELs on silicon photonic integrated circuits", *Manuscript*.

An investigation of angled flip-chip integration of a singlemode 850 nm vertical-cavity surface-emitting laser (VCSEL) on a silicon-nitride (SiN) photonic integrated circuit (PIC) is presented. The VCSEL beam is launched into the SiN waveguide through a grating coupler (GC). Numerical FDTD simulations are done to investigate coupling efficiency and optical back reflection in terms of the VCSEL size and flip-chip angle. Results revealed strong dependence of the coupling efficiency and optical reflection on the VCSEL size and flip-chip angle. Furthermore, we also experimentally demonstrate angled flip-chip integration of GaAs-based 850 nm single transverse and polarization mode VCSELs over GCs on a SiN PIC. At the output GC, light is either collected by an optical fiber or converted to a photocurrent using a flip-chip integrated GaAs-based photodetector (PD). The latter forms an on-PIC optical link. We measured an insertion loss of 21.9, 17.6 and 20.1 dB with a singlemode fiber, multimode fiber and PD over the output grating coupler, respectively.

My contribution: I performed all measurements needed to characterize VCSEL performance before flip-chip integration. I provided all VCSELs to our partner who did the flip-chip integration. After integration, I did all measurements to extract the PIC insertion loss for different optical link schemes, including VCSEL-SMF, VCSEL-MMF, and VCSEL-PD. I co-authored the paper.

References

[1] M. M. Group, "Internet world stats," https://www.internetworldstats.com/stats.htm, accessed 2021-11-01, 2021.

[2] Cisco, "Cisco Global Cloud Index : Forecast and Methodology , 2014-2019," Tech. Rep., 2016. [Online]. Available: https://www.cisco.com/c/dam/en/us/solutions/collateral/service-provider/global-cloud-index-gci/white-paper-c11-738085.pdf

[3] K. Mlitz, "Number of hyperscale data centers worldwide from 2015 to 2020 ," https://www.statista.com/statistics/633826/worldwide-hyperscale-data-center-numbers/, accessed 2021-11-01, 2021.

[4] N. Lehrer, "The largest data centers in the world," https://www.networkcomputing.com/cloud-infrastructure/the-largest-data-canters-in-the-world/d/d-id/1269250, accessed 2015-08-16, 2014.

[5] H. Menear, "Top 10 biggest data centres in the world," https://www.gigabitmagazine.com/top10/top-10-biggest-data-centres-world, accessed 2019-25-06, 2018.

[6] A. Larsson, "Advances in VCSELs for communication and sensing," *IEEE Journal of Selected Topics in Quantum Electronics*, vol. 17.

[7] O. Ueda and S. J. Pearton, *Materials and reliability handbook for semiconductor optical and electron devices*. Springer Science & Business Media, 2012.

[8] H. Blog, "Top of rack swith," https://fspro.hatenablog.com/entry/top-of-rack-switch, accessed 2019-27-06, 2018.

[9] X. Jin, F. Zhang, A. V. Vasilakos, and Z. Liu, "Green data centers: A survey, perspectives, and future directions," *arXiv preprint arXiv:1608.00687*, 2016.

[10] K. Bilal, S. U. R. Malik, O. Khalid, A. Hameed, E. Alvarez, V. Wijaysekara, R. Irfan, S. Shrestha, D. Dwivedy, M. Ali *et al.*, "A taxonomy and survey on green data center networks," *Future Generation Computer Systems*, vol. 36, pp. 189–208, 2014.

[11] M. Al-Fares, A. Loukissas, and A. Vahdat, "A scalable, commodity data center network architecture," *Proc. ACM SIGCOMM Computer Communication Review*, vol. 38, no. 4, pp. 63–74, 2008.

[12] C. Kachris, K. Kanonakis, and I. Tomkos, "Optical interconnection networks in data centers: Recent trends and future challenges," *IEEE Communications Magazine*, vol. 51, no. 9, pp. 39–45, 2013.

[13] L. Wang, F. Zhang, J. A. Aroca, A. V. Vasilakos, K. Zheng, C. Hou, D. Li, and Z. Liu, "GreenDCN: A general framework for achieving energy efficiency in data center networks," *IEEE Journal on Selected Areas in Communications*, vol. 32, no. 1, pp. 4–15, 2013.

[14] A. Vahdat, H. Liu, X. Zhao, and C. Johnson, "The emerging optical data center," *Proc. Optical Fiber Communication Conference*, p. OTuH2, 2011, Optical Society of America.

[15] G. Liu, J. Gao, H. Cheng, H.-C. Wu, E. Lau, L. Yuan, and C. Krause, "Thunderbolt interconnect–comparing optical and copper approaches," *Proc. IEEE International Symposium on Electromagnetic Compatibility & Signal/Power Integrity (EMCSI)*, pp. 305–309, 2017.

[16] H. Cheng, J. Gao, H.-C. Wu, G. Liu, E. Lau, L. Yuan, and C. Krause, "Optics vs. copper, from the perspective of thunderbolt 3 interconnect technology," *Proc. China Semiconductor Technology International Conference (CSTIC)*, pp. 1–3, IEEE, 2016.

[17] M. Freebody, "Lasers evolve to meet the demands of optical communications," *Photonics spectra*, vol. 46, pp. 50–53, 02 2012.

[18] J. A. Tatum, D. Gazula, L. A. Graham, J. K. Guenter, R. H. Johnson, J. King, C. Kocot, G. D. Landry, I. Lyubomirsky, A. N. MacInnes *et al.*, "VCSEL-based interconnects for current and future data centers," *Journal of Lightwave Technology*, vol. 33, no. 4, pp. 727–732, 2015.

[19] P. Westbergh, E. P. Haglund, E. Haglund, R. Safaisini, J. Gustavsso, and A. Larsson, "High-speed 850 nm VCSELs operating error free up to 57 Gbit/s," *Electronics Letters*, vol. 49, no. 16, pp. 1021–1023, 2013.

[20] D. M. Kuchta, A. V. Rylyakov, F. E. Doany, C. L. Schow, J. E. Proesel, C. W. Baks, P. Westbergh, J. S. Gustavsson, and A. Larsson, "A 71 Gbit/s NRZ modulated 850-nm VCSEL-based optical link," *IEEE Photonics Technology Letters*, vol. 27, no. 6, pp. 577–580, 2015.

48

[21] A. Larsson, E. Simpanen, J. Gustavsson, E. Haglund, E. Haglund, T. Lengyel, P. Andrekson, W. Sorin, S. Mathai, M. Tan *et al.*, "1060 nm VCSELs for long-reach optical interconnects," *Optical Fiber Technology*, vol. 44, pp. 36–42, 2018.

[22] M.-J. Li, "Novel optical fibers for data center applications," *Broadband Access Communication Technologies X*, vol. 9772, p. 977205, 2016, International Society for Optics and Photonics.

[23] J. Lavrencik, S. Varughese, J. S. Gustavsson, E. Haglund, A. Larsson, and S. E. Ralph, "Error-free 100Gbps PAM-4 transmission over 100m wideband fiber using 850nm VCSELs," *European Conference on Optical Communication (ECOC)*, pp. 1–3, IEEE, 2017.

[24] S. K. Pavan, J. Lavrencik, R. Shubochkin, Y. Sun, J. Kim, D. Vaidya, R. Lingle, T. Kise, and S. E. Ralph, "50 Gbit/s PAM-4 MMF transmission using 1060nm VCSELs with reach beyond 200m," *Optical Fiber Communication Conference*, pp. W1F–5, Optical Society of America, 2014.

[25] P. Westbergh, J. S. Gustavsson, and A. Larsson, "VCSEL arrays for multicore fiber interconnects with an aggregate capacity of 240 Gbit/s," *IEEE Photonics Technology Letters*, vol. 27, no. 3, pp. 296–299, 2014.

[26] I. Lyubomirsky, R. Motaghian, H. Daghighian, D. McMahon, S. Nelson, C. Kocot, J. Tatum, F. Achten, P. Sillard, D. Molin *et al.*, "100 G SWDM4 transmission over 300m wideband MMF," *European Conference on Optical Communication (ECOC)*, pp. 1–3, IEEE, 2015.

[27] J. Lavrencik, S. Varughese, V. A. Thomas, G. Landry, Y. Sun, R. Shubochkin, K. Balemarthy, J. Tatum, and S. E. Ralph, "4λ× 100 Gbps VCSEL PAM-4 transmission over 105 m of wide band multimode fiber," *Optical Fiber Communication Conference*, pp. Tu2B–6, Optical Society of America, 2017.

[28] J. Lavrencik, S. Varughese, V. A. Thomas, and S. E. Ralph, "Scaling VCSEL-MMF links to 1 Tb/s using short wavelength division multiplexing," *Journal of Lightwave Technology*, vol. 36, no. 18, pp. 4138–4145, 2018.

[29] H. Hatakeyama, T. Anan, T. Akagawa, K. Fukatsu, N. Suzuki, K. Tokutome, and M. Tsuji, "Highly reliable high-speed 1.1 μm-range VCSELs with InGaAs/GaAsP-MQWs," *IEEE Journal of Quantum Electronics*, vol. 46, no. 6, pp. 890–897, 2010.

[30] S. Sweeney, A. Phillips, A. Adams, E. O'reilly, and P. Thijs, "The effect of temperature dependent processes on the performance of 1.5-μm compressively strained InGaAs (P) MQW semiconductor diode lasers," *IEEE Photonics Technology Letters*, vol. 10, no. 8, pp. 1076–1078, 1998.

[31] R. E. Freund, C.-A. Bunge, N. N. Ledentsov, D. Molin, and C. Caspar, "High-speed transmission in multimode fibers," *Journal of Lightwave Technology*, vol. 28, no. 4, pp. 569–586, 2009.

[32] J. A. Kash, A. F. Benner, F. E. Doany, D. M. Kuchta, B. G. Lee, P. K. Pepeljugoski, L. Schares, C. L. Schow, and M. Taubenblatt, "Optical interconnects in exascale supercomputers," *23rd Annual Meeting of the IEEE Photonics Society*, pp. 483–484, IEEE, 2010.

[33] C. Minkenberg, "HPC networks: Challenges and the role of optics," *Optical Fiber Communications Conference and Exhibition (OFC)*, pp. 1–3, IEEE, 2015.

[34] C. J. Chang-Hasnain, M. W. Maeda, J. P. Harbison, L. Florez, and C. Lin, "Monolithic multiple wavelength surface emitting laser arrays," *Journal of lightwave technology*, vol. 9, no. 12, pp. 1665–1673, 1991.

[35] M. Arai, T. Kondo, A. Onomura, A. Matsutani, T. Miyamoto, and F. Koyama, "Multiple-wavelength GaInAs-GaAs vertical cavity surface emitting laser array with extended wavelength span," *IEEE Journal of selected topics in quantum electronics*, vol. 9, no. 5, pp. 1367–1373, 2003.

[36] J. Geske, D. Leonard, M. H. MacDougal, B. Barnes, and J. E. Bowers, "CWDM vertical-cavity surface-emitting laser array spanning 140 nm of the C, S, and L fiber transmission bands," *IEEE Photonics Technology Letters*, vol. 16, no. 5, pp. 1227–1229, 2004.

[37] A. Fiore, Y. Akulova, J. Ko, E. Hegblom, and L. A. Coldren, "Postgrowth tuning of semiconductor vertical cavities for multiple-wavelength laser arrays," *IEEE journal of quantum electronics*, vol. 35, no. 4, pp. 616–623, 1999.

[38] D. Huffaker and D. Deppe, "Multiwavelength, densely-packed 2 × 2 vertical-cavity surface-emitting laser array fabricated using selective oxidation," *IEEE Photonics Technology Letters*, vol. 8, no. 7, pp. 858–860, 1996.

[39] E. Haglund, J. S. Gustavsson, J. Bengtsson, Å. Haglund, A. Larsson, D. Fattal, W. Sorin, and M. Tan, "Demonstration of post-growth wavelength setting of VCSELs using high-contrast gratings," *Optics express*, vol. 24, no. 3, pp. 1999–2005, 2016.

[40] T. Wipiejewski, M. Peters, E. Hegblom, and L. Coldren, "Vertical-cavity surface-emitting laser diodes with post-growth wavelength adjustment," *IEEE photonics technology letters*, vol. 7, no. 7, pp. 727–729, 1995.

[41] S.-Y. Hu, J. Ko, and L. A. Coldren, "High-performance densely packed vertical-cavity photonic integrated emitter arrays for direct-coupled

WDM applications," *IEEE Photonics Technology Letters*, vol. 10, no. 6, pp. 766–768, 1998.

[42] J.-H. Shin and B.-S. Yoo, "Fabrication method for multiple wavelength vertical-cavity emitter arrays by SiN$_x$ layer thickness control," *IEEE Photonics Technology Letters*, vol. 11, no. 5, pp. 509–511, 1999.

[43] P. B. Dayal, T. Sakaguchi, A. Matsutani, and F. Koyama, "Multiple-wavelength vertical-cavity surface-emitting lasers by grading a spacer layer for short-reach wavelength division multiplexing applications," *Applied physics express*, vol. 2, no. 9, p. 092501, 2009.

[44] R. Suzuki, H. Motomura, and S. Satoh, "Vertical cavity surface emitting lasers with precise multi-wavelength control," *International Semiconductor Laser Conference (ISLC)*, pp. 1–2, IEEE, 2016.

[45] Y. Kawakita, K. Takaki, M. Funabashi, S. Imai, and A. Kasukawa, "1060 nm single-mode multi-wavelength VCSEL array with intra-cavity phase tuning layers," *International Semiconductor Laser Conference*, pp. 207–208, IEEE, 2014.

[46] S. Spiga, C. Xie, P. Dong, M.-C. Amann, and P. Winzer, "Ultra-high-bandwidth monolithic VCSEL arrays for high-speed metro networks," *16th International Conference on Transparent Optical Networks (ICTON)*, pp. 1–4, IEEE, 2014.

[47] C. Xie, S. Spiga, P. Dong, P. Winzer, M. Bergmann, B. Kögel, C. Neumeyr, and M.-C. Amann, "400 Gb/s PDM-4PAM WDM system using a monolithic 2×4 VCSEL array and coherent detection," *Journal of Lightwave Technology*, vol. 33, no. 3, pp. 670–677, 2014.

[48] D. Dai, Z. Wang, J. F. Bauters, M.-C. Tien, M. J. Heck, D. J. Blumenthal, and J. E. Bowers, "Low-loss Si$_3$N$_4$ arrayed-waveguide grating (de) multiplexer using nano-core optical waveguides," *Optics express*, vol. 19, no. 15, pp. 14 130–14 136, 2011.

[49] H. Lu, J. S. Lee, Y. Zhao, C. Scarcella, P. Cardile, A. Daly, M. Ortsiefer, L. Carroll, and P. O'Brien, "Flip-chip integration of tilted VCSELs onto a silicon photonic integrated circuit," *Optics express*, vol. 24, no. 15, pp. 16 258–16 266, 2016.

[50] H. Lu, J. S. Lee, Y. Zhao, P. Cardile, A. Daly, L. Carroll, and P. O'Brien, "Hybrid integration of VCSELs onto a silicon photonic platform for biosensing application," *Optical Diagnostics and Sensing XVII: Toward Point-of-Care Diagnostics*, vol. 10072, p. 100720K, International Society for Optics and Photonics, 2017.

[51] A. Haglund, J. S. Gustavsson, J. Vukusic, P. Modh, and A. Larsson, "Single fundamental-mode output power exceeding 6 mw from VCSELs with a shallow surface relief," *IEEE Photonics Technology Letters*, vol. 16, no. 2, pp. 368–370, 2004.

[52] H. Martinsson, J. Vukusic, and A. Larsson, "Single-mode power dependence on surface relief size for mode-stabilized oxide-confined vertical-cavity surface-emitting lasers," *IEEE Photonics Technology Letters*, vol. 12, no. 9, pp. 1129–1131, 2000.

[53] A. Haglund, J. S. Gustavsson, J. Bengtsson, P. Jedrasik, and A. Larsson, "Design and evaluation of fundamental-mode and polarization-stabilized VCSELs with a subwavelength surface grating," *IEEE journal of quantum electronics*, vol. 42, no. 3, pp. 231–240, 2006.

[54] T. H. Maiman, "Stimulated optical radiation in ruby," *Nature*, vol. 187, pp. 493–494, 1960.

[55] M. Noginov, G. Zhu, A. Belgrave, R. Bakker, V. Shalaev, E. Narimanov, S. Stout, E. Herz, T. Suteewong, and U. Wiesner, "Demonstration of a spaser-based nanolaser," *Nature*, vol. 460, no. 7259, pp. 1110–1112, 2009.

[56] L. L. N. Laboratory, "The World's largest and highest-energy laser," https://lasers.llnl.gov/about/what-is-nif, accessed 2021-10-20.

[57] K. Iga, "Surface-emitting laser-its birth and generation of new optoelectronics field," *IEEE Journal of Selected Topics in Quantum Electronics*, vol. 6, no. 6, pp. 1201–1215, 2000.

[58] H. Soda, K.-i. Iga, C. Kitahara, and Y. Suematsu, "GaInAsP/InP surface emitting injection lasers," *Japanese Journal of Applied Physics*, vol. 18, no. 12, p. 2329, 1979.

[59] F. Koyama, S. Kinoshita, and K. Iga, "Room-temperature continuous wave lasing characteristics of a GaAs vertical cavity surface-emitting laser," *Applied physics letters*, vol. 55, no. 3, pp. 221–222, 1989.

[60] J. Jewell, A. Scherer, S. McCall, Y.-H. Lee, S. Walker, J. Harbison, and L. Florez, "Low-threshold electrically pumped vertical-cavity surface-emitting microlasers," *Electronics Letters*, vol. 25, no. 17, pp. 1123–1124, 1989.

[61] Y.-H. Lee, J. Jewell, A. Scherer, S. McCall, J. Harbison, and L. Florez, "Room-temperature continuous-wave vertical-cavity single-quantum-well microlaser diodes," *Electronics Letters*, vol. 25, no. 20, pp. 1377–1378, 1989.

[62] R. Geels, S. Corzine, J. Scott, D. Young, and L. Coldren, "Low threshold planarized vertical-cavity surface-emitting lasers," *Optical Fiber Communication Conference*, p. PD31, Optical Society of America, 1990.

[63] R. S. Geels and L. A. Coldren, "Submilliamp threshold vertical-cavity laser diodes," *Applied physics letters*, vol. 57, no. 16, pp. 1605–1607, 1990.

[64] A. Larsson, "Semiconductor optoelectronics: Device physics and technologies," *Chalmers University of Technology*, 2013.

[65] S. B. Healy, E. P. O'Reilly, J. S. Gustavsson, P. Westbergh, Å. Haglund, A. Larsson, and A. Joel, "Active region design for high-speed 850 nm VCSELs," *IEEE Journal of Quantum Electronics*, vol. 46, no. 4, pp. 506–512, 2010.

[66] L. A. Coldren, S. W. Corzine, and M. L. Mashanovitch, *Diode lasers and photonic integrated circuits*. John Wiley & Sons, 2012, vol. 218.

[67] S. Adachi, *Properties of aluminium gallium arsenide*. IET, 1993, no. 7.

[68] M. Jahed, J. S. Gustavsson, and A. Larsson, "VCSEL wavelength setting by intra-cavity phase tuning–numerical analysis and experimental verification," *IEEE Journal of Quantum Electronics*, 2021.

[69] C. Chang-Hasnain, Y. Wu, G. Li, G. Hasnain, K. Choquete, C. Caneau, and L. Florez, "Low threshold buried heterostructure vertical cavity surface emitting laser," *Applied physics letters*, vol. 63, no. 10, pp. 1307–1309, 1993.

[70] M. Orenstein, A. V. Lehmen, C. Chang-Hasnain, N. Stoffel, J. Harbison, L. Florez, E. Clausen, and J. Jewell, "Vertical-cavity surface-emitting InGaAs/GaAs lasers with planar lateral definition," *Applied physics letters*, vol. 56, no. 24, pp. 2384–2386, 1990.

[71] M.-C. Amann and W. Hofmann, "InP-based long-wavelength VCSELs and VCSEL arrays," *IEEE Journal of Selected Topics in Quantum Electronics*, vol. 15, no. 3, pp. 861–868, 2009.

[72] D. L. Huffaker, D. Deppe, K. Kumar, and T. Rogers, "Native-oxide defined ring contact for low threshold vertical-cavity lasers," *Applied Physics Letters*, vol. 65, no. 1, pp. 97–99, 1994.

[73] N. Dutta, L. Tu, G. Hasnain, G. Zydzik, Y. Wang, and A. Cho, "Anomalous temporal response of gain guided surface emitting lasers," *Electronics Letters*, vol. 27, no. 3, pp. 208–210, 1991.

[74] B. Weigl, M. Grabherr, C. Jung, R. Jager, G. Reiner, R. Michalzik, D. Sowada, and K. J. Ebeling, "High-performance oxide-confined GaAs VCSELs," *IEEE Journal of Selected Topics in Quantum Electronics*, vol. 3, no. 2, pp. 409–415, 1997.

[75] B. E. Saleh and M. C. Teich, *Fundamentals of photonics*. John Wiley & Sons, 2019.

[76] J.-P. Zhang and K. Petermann, "Numerical analysis of transverse mode in gain-guided vertical cavity surface emitting lasers," *IEE Proceedings-Optoelectronics*, vol. 142, no. 1, pp. 29–35, 1995.

[77] Y. Satuby and M. Orenstein, "Mode-coupling effects on the small-signal modulation of multitransverse-mode vertical-cavity semiconductor lasers," *IEEE journal of quantum electronics*, vol. 35, no. 6, pp. 944–954, 1999.

[78] R. Michalzik, *VCSELs: Fundamentals, technology and applications of vertical-cavity surface-emitting lasers*.   Springer, 2012, vol. 166.

[79] Y. Chang, C. Wang, L. Johansson, and L. Coldren, "High-efficiency, high-speed VCSELs with deep oxidation layers," *Electronics Letters*, vol. 42, no. 22, pp. 1281–1282, 2006.

[80] K. Takaki, "A recoded 62% PCE and low series and thermal resistance VCSEL with a double intra-cavity structure," *IEEE International Semiconductor Laser Conf., Sept. 2008*, 2008.

[81] N. Nishiyama, M. Arai, S. Shinada, K. Suzuki, F. Koyama, and K. Iga, "Multi-oxide layer structure for single-mode operation in vertical-cavity surface-emitting lasers," *IEEE Photonics Technology Letters*, vol. 12, no. 6, pp. 606–608, 2000.

[82] S. Adachi, "Lattice thermal resistivity of III–V compound alloys," *Journal of Applied Physics*, vol. 54, no. 4, pp. 1844–1848, 1983.

[83] E. Haglund, P. Westbergh, J. S. Gustavsson, E. P. Haglund, A. Larsson, M. Geen, and A. Joel, "30 GHz bandwidth 850 nm VCSEL with sub-100 fj/bit energy dissipation at 25–50 Gbit/s," *Electronics Letters*, vol. 51, no. 14, pp. 1096–1098, 2015.

[84] J. M. Castro, R. Pimpinella, B. Kose, P. Huang, B. Lane, K. Szczerba, P. Westbergh, T. Lengyel, J. S. Gustavsson, A. Larsson *et al.*, "Investigation of 60 Gbit/s 4-PAM using an 850 nm VCSEL and multimode fiber," *Journal of Lightwave Technology*, vol. 34, no. 16, pp. 3825–3836, 2016.

[85] D. Kuchta, J. Proesel, F. Doany, W. Lee, T. Dickson, H. Ainspan, M. Meghelli, P. Pepeljugoski, X. Gu, M. Beakes *et al.*, "Multi-wavelength optical transceivers integrated on node (MOTION)," *Optical Fiber Communications Conference and Exhibition (OFC)*, pp. 1–3, IEEE, 2019.

[86] R. Baets, A. Z. Subramanian, S. Clemmen, B. Kuyken, P. Bienstman, N. Le Thomas, G. Roelkens, D. Van Thourhout, P. Helin, and S. Severi, "Silicon photonics: Silicon nitride versus silicon-on-insulator," *Optical Fiber Communication Conference*, pp. Th3J–1, Optical Society of America, 2016.

[87] X. Hu, M. Girardi, Z. Ye, P. Muñoz, A. Larsson *et al.*, "Si$_3$N$_4$ photonic integration platform at 1 μm for optical interconnects," *Optics express*, vol. 28, no. 9, pp. 13 019–13 031, 2020.

[88] E. Simpanen, J. Gustavsson, E. Haglund, E. Haglund, A. Larsson, W. Sorin, S. Mathai, and M. Tan, "1060 nm single-mode vertical-cavity surface-emitting laser operating at 50 Gbit/s data rate," *Electronics Letters*, vol. 53, no. 13, pp. 869–871, 2017.

[89] J. S. Gustavsson, Å. Haglund, J. A. Vukušić, J. Bengtsson, P. Jedrasik, and A. Larsson, "Efficient and individually controllable mechanisms for mode and polarization selection in VCSELs, based on a common, localized, sub-wavelength surface grating," *Optics express*, vol. 13, no. 17, pp. 6626–6634, 2005.

[90] Z. Wang, A. Abbasi, U. Dave, A. De Groote, S. Kumari, B. Kunert, C. Merckling, M. Pantouvaki, Y. Shi, B. Tian *et al.*, "Novel light source integration approaches for silicon photonics," *Laser & Photonics Reviews*, vol. 11, no. 4, p. 1700063, 2017.

[91] D. Houghton, J.-P. Noël, and N. Rowell, "Si-based photonic devices by MBE," *MRS Online Proceedings Library Archive*, vol. 220, 1991.

[92] G. Abstreiter, "Engineering the future of electronics," *Physics World*, vol. 5, no. 3, p. 36, 1992.

[93] R. A. Soref, "Silicon-based optoelectronics," *Proceedings of the IEEE*, vol. 81, no. 12, pp. 1687–1706, 1993.

[94] C. R. Doerr, "Silicon photonic integration in telecommunications," *Frontiers in Physics*, vol. 3, p. 37, 2015.

[95] A. Novack, M. Streshinsky, T. Huynh, T. Galfsky, H. Guan, Y. Liu, Y. Ma, R. Shi, A. Horth, Y. Chen *et al.*, "A silicon photonic transceiver and hybrid tunable laser for 64 Gbaud coherent communication," *Optical Fiber Communication Conference*, pp. Th4D–4, Optical Society of America, 2018.

[96] G. Roelkens, A. Abassi, P. Cardile, U. Dave, A. De Groote, Y. De Koninck, S. Dhoore, X. Fu, A. Gassenq, N. Hattasan *et al.*, "III-V-on-silicon photonic devices for optical communication and sensing," *Photonics*, vol. 2, no. 3, pp. 969–1004, Multidisciplinary Digital Publishing Institute, 2015.

[97] A. Z. Subramanian, E. Ryckeboer, A. Dhakal, F. Peyskens, A. Malik, B. Kuyken, H. Zhao, S. Pathak, A. Ruocco, A. De Groote *et al.*, "Silicon and silicon nitride photonic circuits for spectroscopic sensing on-a-chip," *Photonics Research*, vol. 3, no. 5, pp. B47–B59, 2015.

[98] S. Wirths, R. Geiger, N. Von Den Driesch, G. Mussler, T. Stoica, S. Mantl, Z. Ikonic, M. Luysberg, S. Chiussi, J.-M. Hartmann *et al.*, "Lasing in direct-bandgap GeSn alloy grown on Si," *Nature photonics*, vol. 9, no. 2, pp. 88–92, 2015.

[99] T. Shimizu, N. Hatori, M. Kurihara, Y. Urino, T. Yamamoto, T. Nakamura, and Y. Arakawa, "Optical characteristics of a multichannel hybrid integrated light source for ultra-high-bandwidth optical interconnections," *Photonics*, vol. 2, no. 4, pp. 1131–1138, Multidisciplinary Digital Publishing Institute, 2015.

[100] Y.-Q. Bie, G. Grosso, M. Heuck, M. M. Furchi, Y. Cao, J. Zheng, D. Bunandar, E. Navarro-Moratalla, L. Zhou, D. K. Efetov *et al.*, "A mote 2-based light-emitting diode and photodetector for silicon photonic integrated circuits," *Nature nanotechnology*, vol. 12, no. 12, pp. 1124–1129, 2017.

[101] G. Roelkens, L. Liu, D. Liang, R. Jones, A. Fang, B. Koch, and J. Bowers, "III-V/silicon photonics for on-chip and intra-chip optical interconnects," *Laser & Photonics Reviews*, vol. 4, no. 6, pp. 751–779, 2010.

[102] A. Plößl and G. Kräuter, "Wafer direct bonding: Tailoring adhesion between brittle materials," *Materials Science and Engineering: R: Reports*, vol. 25, no. 1-2, pp. 1–88, 1999.

[103] M. Wiemer, C. Jia, M. Toepper, and K. Hauck, "Wafer bonding with BCB and SU-8 for MEMS packaging," *1st Electronic Systemintegration Technology Conference*, vol. 2, pp. 1401–1405, IEEE, 2006.

[104] J. Zhang, G. Muliuk, J. Juvert, S. Kumari, J. Goyvaerts, B. Haq, C. Op de Beeck, B. Kuyken, G. Morthier, D. Van Thourhout *et al.*, "III-V-on-Si photonic integrated circuits realized using micro-transfer-printing," *APL photonics*, vol. 4, no. 11, p. 110803, 2019.

[105] R. Marchetti, C. Lacava, L. Carroll, K. Gradkowski, and P. Minzioni, "Coupling strategies for silicon photonics integrated chips," *Photonics Research*, vol. 7, no. 2, pp. 201–239, 2019.

[106] T. Pinguet, S. Denton, S. Gloeckner, M. Mack, G. Masini, A. Mekis, S. Pang, M. Peterson, S. Sahni, and P. De Dobbelaere, "High-volume manufacturing platform for silicon photonics," *Proceedings of the IEEE*, vol. 106, no. 12, pp. 2281–2290, 2018.

[107] Y. Wang, S. S. Djordjecvic, J. Yao, J. E. Cunningham, X. Zheng, A. V. Krishnamoorthy, M. Muller, M.-C. Amann, R. Bojko, N. A. Jaeger *et al.*, "Vertical-cavity surface-emitting laser flip-chip bonding to silicon photonics chip," *IEEE Optical Interconnects Conference (OI)*, pp. 122–123, IEEE, 2015.

[108] K. Kaur, A. Subramanian, P. Cardile, R. Verplancke, J. Van Kerrebrouck, S. Spiga, R. Meyer, J. Bauwelinck, R. Baets, and G. Van Steenberge, "Flip-chip assembly of VCSELs to silicon grating couplers via laser fabricated SU-8 prisms," *Optics express*, vol. 23, no. 22, pp. 28 264–28 270, 2015.

[109] Z. Ruan, Y. Zhu, P. Chen, Y. Shi, S. He, X. Cai, and L. Liu, "Efficient hybrid integration of long-wavelength VCSELs on silicon photonic circuits," *Journal of Lightwave Technology*, vol. 38, no. 18, pp. 5100–5106, 2020.

[110] J. Y. Law and G. P. Agrawal, "Effects of optical feedback on static and dynamic characteristics of vertical-cavity surface-emitting lasers," *IEEE Journal of Selected Topics in Quantum Electronics*, vol. 3, no. 2, pp. 353–358, 1997.

[111] Europractice, "—," https://europractice-ic.com/mpw-prototyping/siphotonics/imec/, accessed 2021-11-08.